AGU PUBLICATIONS

JGR

Journal of Geophysical Research: Solid Earth

RESEARCH ARTICLE
10.1002/2015JB012245

Key Points:
- We review techniques for measurements of hydrothermal discharge at ocean floor depths
- We describe new instruments for measuring fluid flow and heat output
- We report 120 new measurements at Juan de Fuca Ridge, East Pacific Rise, and Lau Basin

Correspondence to:
L. N. Germanovich,
leonid@ce.gatech.edu

Citation:
Germanovich, L. N., R. S. Hurt, J. E. Smith, G. Genc, and R. P. Lowell (2015), Measuring fluid flow and heat output in seafloor hydrothermal environments, *J. Geophys. Res. Solid Earth*, *120*, 8031–8055, doi:10.1002/2015JB012245.

Received 2 JUN 2015
Accepted 2 JUN 2015
Accepted article online 24 JUL 2015
Published online 19 DEC 2015

Measuring fluid flow and heat output in seafloor hydrothermal environments

Leonid N. Germanovich[1], Robert S. Hurt[1,2], Joshua E. Smith[1], Gence Genc[1,3], and Robert P. Lowell[4]

[1]School of Civil and Environmental Engineering, Georgia Institute of Technology, Atlanta, Georgia, USA, [2]Now at Baker Hughes, Houston, Texas, USA, [3]Now at Department of Civil Engineering, Çankaya University, Ankara, Turkey, [4]Department of Geosciences, Virginia Polytechnic Institute and State University, Blacksburg, Virginia, USA

Abstract We review techniques for measuring fluid flow and advective heat output from seafloor hydrothermal systems and describe new anemometer and turbine flowmeter devices we have designed, built, calibrated, and tested. These devices allow measuring fluid velocity at high- and low-temperature focused and diffuse discharge sites at oceanic spreading centers. The devices perform at ocean floor depths and black smoker temperatures and can be used to measure flow rates ranging over 2 orders of magnitude. Flow velocity is determined from the rotation rate of the rotor blades or paddle assembly. These devices have an open bearing design that eliminates clogging by particles or chemical precipitates as the fluid passes by the rotors. The devices are compact and lightweight enough for deployment from either an occupied or remotely operated submersible. The measured flow rates can be used in conjunction with vent temperature or geochemical measurements to obtain heat outputs or geochemical fluxes from both vent chimneys and diffuse flow regions. The devices have been tested on 30 *Alvin* dives on the Juan de Fuca Ridge and 3 *Jason* dives on the East Pacific Rise (EPR). We measured an anomalously low entrainment coefficient (0.064) and report 104 new measurements over a wide range of discharge temperatures (5°–363°C), velocities (2–199 cm/s), and depths (1517–2511 m). These include the first advective heat output measurements at the High Rise vent field and the first direct fluid flow measurement at Middle Valley. Our data suggest that black smoker heat output at the Main Endeavour vent field may have declined since 1994 and that after the 2005–2006 eruption, the high-temperature advective flow at the EPR 9°50′N field may have become more channelized, predominately discharging through the Bio 9 structure. We also report 16 measurements on 10 *Alvin* dives and 2 *Jason* dives with flow meters that predate devices described in this work and were used in the process of their development. This includes the first advective measurements in the Lau Basin and at the EPR 9°39.5′N. We discuss potential error sources and how they may affect the accuracy of measurements by our devices and other devices. In particular, we use the turbulent plume theory to evaluate the effect of entrainment of ambient seawater.

1. Introduction

The discovery of low-temperature hydrothermal discharge at the Galapagos Spreading Center in 1977 [*Corliss et al.*, 1979] and high-temperature "black smoker" vents a year later on the East Pacific Rise (EPR) [*Spiess et al.*, 1980], together with their associated biological ecosystems [*Corliss et al.*, 1979], ushered in a new era of marine geophysical exploration at oceanic spreading centers. Since these discoveries, numerous methods have been used to estimate heat flow from both high-temperature and low-temperature discharge zones [e.g., *Converse et al.*, 1984; *Baker and Massoth*, 1987; *Thomson et al.*, 1992; *Ginster et al.*, 1994; *Schultz et al.*, 1992; *Ramondenc et al.*, 2006].

The high-temperature fluids vent from discrete orifices, whereas low- to moderate-temperature diffuse fluids discharge from nearby patches of seafloor or from sulfide edifices on which the high-temperature vents reside. Diffuse flow discharges that occur at EPR, the Galapagos Spreading Center, and elsewhere have chemical signatures indicating that they are mixtures of high-temperature fluid and seawater [e.g., *Edmond et al.*, 1979; *Corliss et al.*, 1979; *Cooper et al.*, 2000; *Von Damm and Lilley*, 2004; *Lang et al.*, 2006]. Flow data from diffuse sites are necessary for understanding the geochemical and nutrient fluxes to seafloor biological communities, which are required for comprehending ecosystem maintenance and evolution [*Butterfield et al.*, 2004; *Von Damm and Lilley*, 2004; *Wankel et al.*, 2011]. Advective heat transfer data from both diffuse and focused flow sites are critical for understanding the physical and geochemical evolution of seafloor hydrothermal systems [e.g., *Lowell and Germanovich*, 1994, 2004]. These data provide important

constraints on mathematical models that relate magmatic and hydrothermal heat fluxes [e.g., *Lowell and Germanovich*, 2004; *Liu and Lowell*, 2009; *Germanovich et al.*, 2011; *Lowell et al.*, 2013].

Measurements of hydrothermal heat flux can be categorized into two broad classes: direct measurements from discrete vents and integrated water column measurements that are made on the scale of a vent field. In this paper, we first review techniques for measuring advective heat output from seafloor hydrothermal systems. Then, we describe new devices for making direct measurements of fluid flow and heat output and discuss results of their testing during 30 dives on submersible *Alvin* and 3 dives with ROV *Jason*. We also report measurements on 10 *Alvin* and 2 *Jason* dives with devices that predate those described in this work.

2. Measurements of Advective Heat Output From Seafloor Hydrothermal Systems

2.1. Integrated Measurements

Hydrothermal discharge from discrete high-temperature vents forms turbulent buoyant plumes that transfer mass and energy up to several hundred meters above the seafloor [*Middleton and Thomson*, 1986; *Dymond et al.*, 1988; *Speer and Rona*, 1989]. As plumes rise in the water column, they entrain denser ambient seawater. Eventually, they reach their level of neutral buoyancy and spread laterally [e.g., *Morton et al.*, 1956; *Turner and Campbell*, 1987; *Woods*, 2010].

Integrated heat output measurements from a hydrothermal vent field on the seafloor have been made in neutrally buoyant plumes at various locations including the Flow and Floc vent areas at the CoAxial segment [*Baker et al.*, 1998], at the Endeavour segment [*Baker and Massoth*, 1987; *Thomson et al.*, 1992], and North Cleft segment [*Baker et al.*, 1993] of the Juan de Fuca Ridge (JdF), and Broken Spur [*Murton et al.*, 1999] and Trans-Atlantic Geotraverse (TAG) [*Rudnicki and Elderfield*, 1992] hydrothermal fields at the Mid-Atlantic Ridge. Typically, data are collected at the scale of a vent field by conductivity-temperature-depth and transmissometer tows or vertical casts and water bottle sampling through the plume and the ambient ocean [*Baker and Massoth*, 1987; *Thomson et al.*, 1992; *Gendron et al.*, 1994; *Baker et al.*, 1998]. These data are used to determine the maximum rise height in the plume z_{max} and to construct the background density profile $\rho_a(z)$, where z is height above the plume source. One can also use the excess heat content in the neutrally buoyant plume and the advective transport velocity of the plume to estimate the heat output from a vent field [e.g., *Baker and Massoth*, 1987; *Thomson et al.*, 1995]. Integrated heat output estimates have also been obtained at the Main Endeavour Field (MEF) on the JdF using the Autonomous Benthic Explorer [*Veirs et al.*, 2006].

The fundamental theory for rise and spreading of turbulent buoyant plumes is outlined by *Morton et al.* [1956] and reviewed by *Fischer et al.* [1979], *Turner* [1986], and *Hunt and van den Bremer* [2011] among others. The theory shows that for a buoyant axisymmetric plume rising from a point source with negligible momentum, $z_{max} = 5(B_0/\pi)^{1/4}N^{-3/4}$, where $B_0 = \alpha_T g H_0/(c_p \rho_0)$ is the buoyancy flux at the source; $N = [(g/\rho_0)(-\mathrm{d}\rho_a/\mathrm{dz})]^{1/2}$ is the buoyancy frequency; g is the gravitational acceleration; ρ_0 and H_0 are the fluid density and the total heat flux at the source, respectively; α_T is the coefficient of thermal expansion of seawater at ambient, low-temperature conditions; c_p is the fluid specific heat at constant pressure; and the density gradient $\mathrm{d}\rho_a/\mathrm{dz}$ in the ambient stratified environment is assumed to be constant. These expressions result in $H_0 = [\pi \rho_0 c_p/(\alpha_T g)](z_{max}/5)^4 N^3$ [e.g., *Baker*, 1994; *Thomson et al.*, 1995], indicating that the heat output is very sensitive to estimates of z_{max} and $\mathrm{d}\rho_a/\mathrm{dz}$. As a result, heat outputs obtained from measurements in the neutrally buoyant plume are uncertain by at least a factor of 2 [e.g., *Baker*, 2007].

Speer and Rona [1989] apply the buyout plume theory to plumes rising in the ocean where the ambient density structure depends upon both temperature and salinity. *Speer and Helfrich* [1995] discuss the effects of cross currents and Coriolis effects and conclude that buoyant plumes can drive ocean circulation at larger scales.

2.2. Direct Measurements

Direct measurements refer to a class of measurements made at a discrete venting site near the seafloor, whether from a high-temperature chimney orifice or a low-temperature diffuse flow site. Direct measurements also include those made in the buoyant plume at some height above individual vents. To obtain the heat output from a vent field, measurements are summed over the discrete sources of fluid discharge,

often extrapolating from a relatively small number of actual measurements to the vent field scale [e.g., *Little et al.*, 1987; *Rona and Trivett*, 1992; *Bemis et al.*, 1993; *Ramondenc et al.*, 2006].

2.2.1. Direct Measurements in Buoyant Plumes

A number of techniques have been used to estimate hydrothermal heat output from measurements within buoyant plumes rising above discrete vents. For example, *Little et al.* [1987] and *Bemis et al.* [1993] used a package of instruments deployed from a submersible to obtain profiles of temperature, velocity, conductivity, and pressure. Ambient stratification was monitored by the instrument array during the descent of the submersible through the water column, whereas the turbulent fluctuations were recorded as a function of time once the submersible was stabilized at a vent site. Because the velocity and temperature in the buoyant plume were measured directly, *Little et al.* [1987] and *Bemis et al.* [1993] applied classic plume theory [*Morton et al.*, 1956; *Tennekes and Lumley*, 1972; *Turner*, 1986; *Fischer et al.*, 1979; *Papanicolaou and List*, 1987] to determine heat flow from individual discrete vents.

Although direct measurements in plumes are an effective way to quantify heat output from discrete high-temperature vents, it is difficult to use plume methods to obtain heat output from diffuse flow sites. Diffuse discharge, because of its lower buoyancy flux, tends to rise relatively short distances above the seafloor [e.g., *Rona and Trivett*, 1992], where it contributes to the warming of the local bottom water. Still, diffuse flow may account for a large fraction of the total heat output from a vent field [e.g., *Schultz et al.*, 1992; *Ramondenc et al.*, 2006]. It is noteworthy, however, that integrated heat output measurements in the neutrally buoyant plume typically exceed estimates made from direct measurements in high-temperature buoyant plumes [e.g., *Baker*, 2007]. This suggests that mixing in the deep ocean changes the density structure such that measurements in the neutrally buoyant plume contain some heat output that results from diffuse flow.

2.2.2. Acoustic and Optical Measurements

Acoustic methods have also been used to image and quantify hydrothermal flow both from diffuse flow sources and discrete vents in the plumes. Such methods have varied from backscattering of an acoustic pulse by small suspended particles [*Palmer*, 2005; *Palmer and Rona*, 2005] or turbulent temperature fluctuations [*Ross and Lueck*, 2003; *Ostachev and Wilson*, 2015] to the use of a Doppler effect to measure flow velocity and mean vertical velocity [*Jackson et al.*, 2003]. An alternative method, the acoustic scintillation from forward scattered signals, has been applied at the MEF [*Xu and Di Iorio*, 2011; *Di Iorio et al.*, 2012] to monitor integrated plumes and investigate temporal variability in physical properties such as temperature or flow velocity. This method is based on recovering properties of the medium by measuring fluctuations of the acoustic signal passing through the plume [*Di Iorio et al.*, 2005]. Using this method, *Xu and Di Iorio* [2011] estimated the heat transport of a plume 20 m above an orifice on Dante at the MEF as 62 MW.

Crone et al. [2008] describe a visual image-based technique to estimate the velocity in a turbulent plume (such as a black smoker) that they term optical plume velocimetry. They apply the method to laboratory experiments and conclude that temporal cross correlation of adjacent pixels provides sensitive estimates of mean flow velocity in the plume. *Crone and Tolstoy* [2010] applied this method to assess the New Horizon oil spill in the Gulf of Mexico.

2.2.3. Eddy and Particle Tracking

Macdonald et al. [1980] and *Rona and Trivett* [1992] estimated the flow velocity in a black smoker plume at 21°N on the EPR and at the ASHES (Axial Seamount Hydrothermal Emissions Study) hydrothermal field at JdF, respectively, by tracking an eddy or a particle against a marked vertical rod. *Ramondenc et al.* [2006] utilized a horizontal stainless steel plate held directly over the vent flow. A circular hole in the center of the plate sampled a portion of the vent flow. The rise time of particles entrained in the fluid emerging through the hole was determined by using a video record to track the particle displacement against a vertical scale attached to the device. Figure 1a shows a similar device deployed at MEF (measurement 3 in Table 1).

Although these devices are relatively simple to use, uncertainties arise because only a limited number of particles can be observed unambiguously, and flow turbulence makes it difficult to accurately determine a particle's rise time. This may have contributed to a large difference in the results of different works. For example, *Macdonald et al.* [1980] obtained heat output from an individual orifice at EPR 21°N as high as 250 MW. Although *Macdonald* [1983] later adjusted this flux value to ≈60 MW, by noting that the measured edifice had four chimneys rather than only one, it still exceeds the results of the subsequent flowmeter measurements of *Converse et al.* [1984] (0.5–10 MW at EPR 21°N; see the next section) by 1 to 2

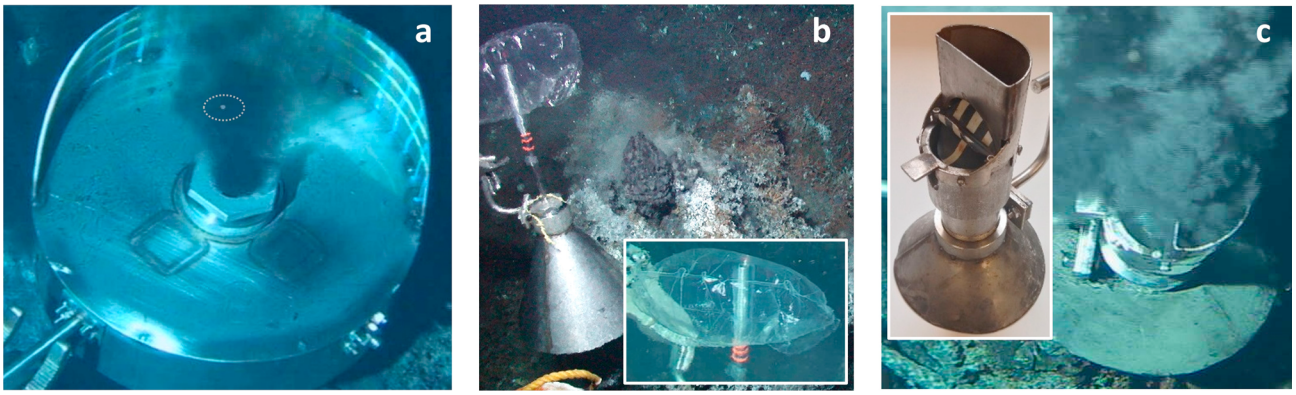

Figure 1. (a) Flow velocity measurement at a black smoker orifice on Dante, MEF, JdF (*Alvin* dive 4350). A particle is tracked on the frames of the video during the dive. Flow rate of the 330°C hydrothermal fluid from the orifice of 5 cm diameter was 20 cm/s, while the heat output was 0.5 MW (measurement 3 in Table 1). (b) Hydrological seepage meter modified for the hydrothermal flow conditions at the ocean floor and deployed vertically over a small chimney during *Alvin* dive 4411 to Dante, MEF, JdF. Flow rate of the 80°C hydrothermal fluid from the orifice of 1 cm diameter was 2 cm/s, while the heat output was only 0.5 kW (measurement 1 in Table 1). Hydrothermal fluid is captured by a collection bag (inset). (c) Anemometer device (inset) that predates the cup anemometer developed in this work (section 3). The paddle rotates on an axis of 5 cm. The device is deployed on the Bio 9 structure, EPR 9°50′N, during *Alvin* dive 4403 (measurement 11 in Table 1).

Table 1. Results of Flow Rate and Heat Output Measurements at the Main Endeavour Field and Middle Valley, JdF Ridge, and at Lau Basin Performed With Devices That Preceded Flowmeters Described in This Work

Alvin Dive	Measurement Number	Depth (m)	Flow Regime	Flow Velocity (cm/s)	Temperature (°C)	Orifice Diameter (cm)	Source Area (cm^2)	Flow Rate (cm^3/s)	Heat Output (kW)
				Main Endeavour Vent Field (Endeavour)					
Dante (47°56.9527N, 129°5.8793′W)									
4411	1	2,192	Focused	2.0[a]	80	1	0.8	1.6	0.5
4348	2	2,176	Focused	24.6[b]	333	6.2	30.2	743	984
4350	3	2,181	Focused	19.9[b]	330	5	19.6	390	512
4350	4	2,181	Focused	36.8[b]	312	4	12.6	464	575
				Middle Valley					
Puppy Dog Mound (48°26.8778′N, 128°42.2538′W)									
4351	5	2,414	Focused	19.6[b]	269	5	19.6	384	410
				Lau Basin					
Marker 7, Tow Cam Vent Field (20°19.001725′S, 176°8.176817′W)									
233[d]	6	2,704	Focused	116[b]	318.6	4	12.6	1,460	1,850
233[d]	7	2,706	Focused	37[b]	316.9	3	7.1	263	331
Site 8, ABE (20°45.983507′S, 176°11.586715′W)									
234[d]	8	2,132	Focused	58[b]	289.1	3	7.1	412	473
234[d]	9	2,130	Focused	100[b]	350	6	28.3	2,830	3,940
				East Pacific Rise					
9°39.5′N (9°39.5344′N, 104°15.7147′W)									
4280	10	2,543	Focused	110[b]	378	4	12.6	1,390	2,090
Bio 9 (9°50.3056′N, 104°17.4764′W)									
4403	11	2,506	Focused	74[c]	341	6	28.3	2,090	2,840
4405	12	2,509	Focused	33[c]	358	3	7.1	234	334
4407	13	2,501	Focused	40[c]	350	3	7.1	284	395
P-vent (9°50.2720′N, 104°17.4640′W)									
4403	14	2,506	Focused	71[c]	374	5	19.6	1,390	2,070
4575	15	2,509	Diffuse	2.0[b]	20[e]		1,850	3,700	268
Tica (9°50.3981′N, 104°17.4927′W)									
4580	16	2,512	Diffuse	5.8[b]	20[e]		1,220	7,080	512

[a]Velocity measured with a seepage meter (Figure 1b) modified to hydrothermal flow conditions at mid-oceanic ridges.
[b]Velocity measured using the particle tracer (Figure 1a).
[c]Velocity measured using an anemometer device (Figure 1c) that predated the cup anemometer (section 3).
[d]*Jason* dives.
[e]Temperature is inferred from additional measurements at the same vent.

orders of magnitude. Nevertheless, these devices have provided important baseline data for flow velocities at both JdF and EPR hydrothermal sites.

2.2.4. Flowmeters

Converse et al. [1984] and *Ginster et al.* [1994] employed a commercial, electromagnetic turbine flowmeter to measure fluid flow at black smoker vents at EPR and JdF, respectively. The flowmeter was deployed from *Alvin* by positioning it a few centimeters above the high-temperature chimney orifices, along the centerline of hydrothermal plumes.

Sarrazin et al. [2009] used a dual-sensor system that combines two methods to estimate diffuse flow rates. A "flow visualizer" consisting of a transparent graduated pipe was placed atop a cylindrical chamber containing a constant voltage anemometer [*King*, 1914]. Similar to *Macdonald et al.* [1980], *Rona and Trivett* [1992], and *Ramondenc et al.* [2006], observations of vertical particle ascent in the pipe were obtained through video imagery.

Schultz et al. [1992, 1996] developed both nonmechanical (using electromagnetic induction) and mechanical (a spinning rotor) meters for measuring diffuse effluent velocities and temperatures. The *Schultz et al.* [1992, 1996] devices could be left in place for days in order to obtain a time series of hydrothermal flow velocity and temperature. *Schultz et al.* [1992] conducted the first direct measurements of diffuse flow on the Peanut structure in the southern part of the MEF.

The major issue associated with heat flow measurements using turbine flowmeters has been the failure of electronic components [e.g., *Converse et al.*, 1984; *Converse*, 1985] and particle precipitation in high-temperature venting [*Ginster et al.*, 1994], which typically coats the turbine blades and jams the bearings.

2.3. Rationale for New Direct Measurement Devices

Although integrated water column measurements provide a useful estimate of the total heat output from a hydrothermal vent field, they do not provide insight into the partitioning between focused and diffuse flow components. Direct fluid flow measurements, when linked with geochemical data, also provide estimates of geochemical fluxes [*Wankel et al.*, 2011]. These fluxes are important for understanding interactions between the hydrothermal processes in oceanic crust and ocean chemistry. Because many of the chemical constituents in hydrothermal fluids are used by microbial and macrofaunal communities, flux data may provide new understanding of the spatial and temporal characteristics of biological processes at oceanic spreading centers [*Wankel et al.*, 2011]. Integrated water column measurements may not have sufficient resolution to characterize individual flow sources that often contribute to the same plume higher in the water column [e.g., *Bemis et al.*, 2002; *Di Iorio et al.*, 2012].

One goal for developing relatively simple devices for direct measurements is for these devices to be part of the standard "tool box" on occupied submersibles such as *Alvin* [e.g., *Rona*, 1999] and remotely operated vehicles (ROVs) such as *Jason* [e.g., *Yoerger et al.*, 1986]. These devices would be relatively compact and lightweight and sufficiently robust for deployment on cruises exploring hydrothermal flows at oceanic spreading centers or flows of a different nature such as petroleum leaks [e.g., *Crone and Tolstoy*, 2010; *Camilli et al.*, 2011]. As such devices become more widely used, the database for heat and biogeochemical fluxes would grow with time.

Most of the methods for heat flow measurements described in the previous sections are either sophisticated [e.g., *Schultz et al.*, 1992, 1996; *Sarrazin et al.*, 2009] or simplistic [e.g., *Macdonald et al.*, 1980; *Rona and Trivett*, 1992; *Ramondenc et al.*, 2006]. Although sophisticated instruments are designed to obtain high-quality data, they are relatively expensive and require high levels of control and maintenance and hence are not used on a routine basis. Methods such as particle tracking have considerable uncertainties because particles entrained in turbulent eddies may not have straight paths and the particles are frequently obscured in the centerline region of the plume flow. In addition, these methods require significant effort in procuring data because the number of visible particles may be too small [*Ramondenc et al.*, 2006]. The earlier turbine flow device [*Converse et al.*, 1984; *Ginster et al.*, 1994] encountered maintenance problems mostly related to the failure of the electronic components and/or coating and clogging of the bearings by accumulated vent or sediment particles.

Flow rate measurements can also be done using a seepage meter [e.g., *Rosenberry*, 2008; L. C. Murdoch, private communication, 2008] modified to ocean floor hydrothermal flow conditions (Figure 1b). Using this

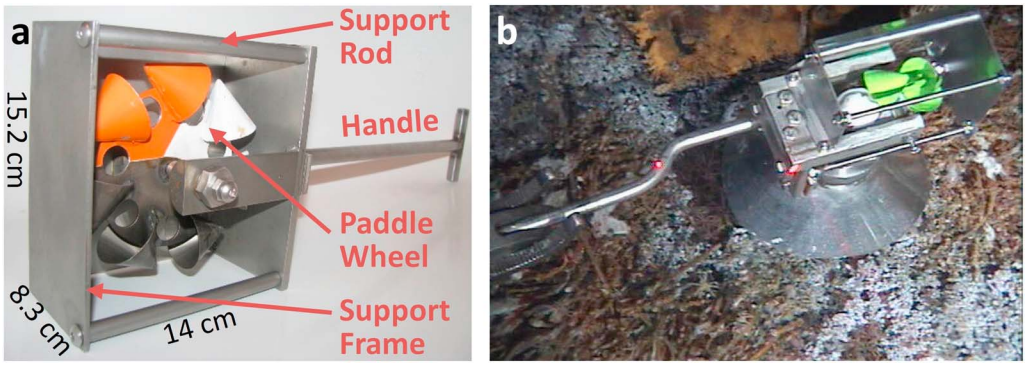

Figure 2. (a) Cup anemometer device. The paddle wheel and anemometer cups are fabricated from a titanium alloy; all other parts are made from stainless steel grade 316. Cups of the paddle wheel were painted to enhance the visualization process. A handle is attached to the frame for deployment from an occupied submersible or ROV. (b) Cup anemometer device deployed at a diffuse flow site (Dante, MEF, *Alvin* dive 4411).

meter results in reliable data (measurement 1 in Table 1); however, the seepage meter can only be used once per dive (at least, without sophisticated changes), which limits its applicability. This is not an issue for the anemometer flow meter (Figure 1c) we developed and used on several occasions. In this meter, the rotor axis is perpendicular to the flow and is supported by jewel bearings we used in the subsequent designs (section 3). The meter is particularly easy to use in transparent or semi-transparent flows (such as white or grey smokers and diffuse flow). In black smoker flows, however, the rotations are difficult to register visually (although not impossible; Table 1, measurements 11–14).

In this paper, we describe three new instruments for making direct measurements of fluid flow in seafloor hydrothermal systems. One is based on a cup anemometer design used in hydrological flow measurements [e.g., *Futrell*, 1989; *Vaughn et al.*, 2006] and the other two are turbine flowmeters, similar to those employed for flow measurements in pipes [e.g., *Munson et al.*, 2005]. When designing these instruments, our main objective was to develop robust, lightweight, and affordable devices, which could operate at high-pressure and high-temperature subsea conditions, would be easy to maintain on shipboard, and would allow reliable flow visualization in both focused and diffuse environments. Below we describe these instruments and report measurement results that show their capabilities. Regardless of fluid temperature, *focused flow* regime refers to sites with a discrete source area and *diffuse flow* regime applies to measurements made on obscured source areas.

3. Fluid Flow Instruments and Methods

3.1. Cup Anemometer

The cup anemometer device consists of a frame and a paddle wheel assembly with a number of attached conical cups. The paddle wheel assembly is mounted on a shaft and rotates freely. The support frame is attached to the metal shield by two support rods. The device is shown in Figures 2 and 3. The paddle wheel assembly was fabricated from a grade 5 titanium alloy [*ASTM*, 2011] to reduce the weight and decrease the potential of corrosion. All other parts are made from grade 316 stainless steel [e.g., *ASTM*, 2010] in order to withstand the high-pressure and high-temperature conditions on the seafloor, in both diffuse and focused flow settings. The rotating wheel has an external diameter of 9.4 cm and has seven cups on its body. Occasionally, a conical flux concentrator (Figures 2b, 3a, and 3c) was attached to the base in order to focus the flow to the anemometer. In the case of diffuse flow, the flow was calculated by backtracking to the full area at the cone base (similar to *Sarrazin et al.* [2009]). For focused flow, the concentrator covered the vent orifice, so that the flow was exiting the orifice near the main part of the device (Figure 3c). On two cruises to JdF in 2008, 64 flow measurements were obtained using this instrument (section 6). The device has dimensions of $15.2 \times 14 \times 8.3$ cm, and it weighs 1.9 and 2.1 kg in room temperature water and air, respectively.

The main difference between our device and those used in hydrological flow measurements [e.g., *Futrell*, 1989; *Vaughn et al.*, 2006] is that we implemented an *open* bearing support. That is, the axis of rotation is

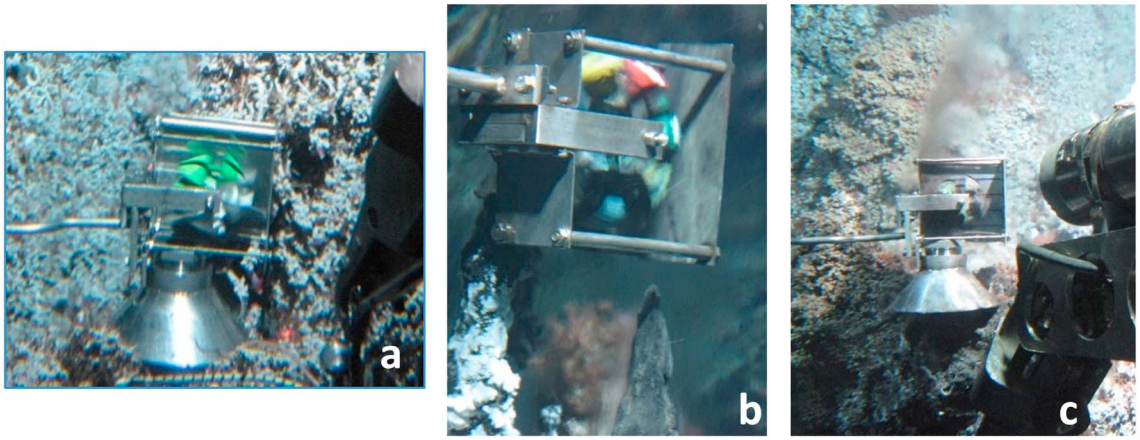

Figure 3. Deployment of the cup anemometer (a) over a low-temperature diffuse flow site (covered with tubeworms) on *Alvin* dive 4412 at the Clam Bed vent field, Endeavour segment, JdF (measurement 61 in Table 2), (b) over a white smoker chimney on *Alvin* dive 4452 to Hulk, MEF (measurement 47 in Table 2), and (c) over a black smoker orifice on *Alvin* dive 4414 to Hulk, MEF (measurement 33 in Table 2). The black smoker flow is affected by cross flow upon exiting the device. Near the orifice, however, the device walls protect the flow (once the device is properly oriented) making the measurements closer to the calibration conditions (section 4).

supported by sapphire jewel bearings [e.g., *Insley et al.*, 1947] that are open to the flow. These bearings are similar to those used in the turbine flowmeter and described in more detail in the next section.

The device is deployed over the fluid discharge site (Figure 3) from either a manned submersible or ROV. The flow into the anemometer is recorded by the submarine's video cameras. The device is typically held at a given site for a few minutes to insure that a sufficient number of revolutions are recorded. The rotation rate is determined postdive from video records by counting paddle wheel rotations within a certain amount of time. Linear flow velocity is obtained from the calibration curve constructed from lab test results (section 4).

The hydrothermal heat output is calculated over the area of an individual chimney orifice or diffuse flow site from

$$H = C_f v(T_f - T_a)A \tag{1}$$

where $C_f \approx 4 \times 10^6$ J/(m^3 × °C) is the volumetric heat capacity of the fluid ($C_f = C_p\rho_f$) [e.g., *Sun et al.*, 2008; *Sharqawy et al.*, 2010]. v is the fluid velocity, $T_f - T_a$ is the difference in temperature between that of hydrothermal vent fluid, T_f, and ambient seawater, T_a, and A is the area of the discharge site, such as a black smoker orifice or patch of diffuse flow. Temperatures T_f and T_a are directly measured by the submarine's temperature sensor. The orifice sizes are estimated from video footage using *Alvin*'s red laser beams (spaced at the fixed distance of 10 cm; see also caption to Figure 7) and other appropriately oriented scales such as marked metal rods or the jaws of *Alvin*'s manipulators. In the case of black smokers, it is rare when the inner side of the orifice can actually be seen, but in several occasions, we were able to bring the upper part of the chimney on board and compare the actual orifice geometry, determined by slicing the samples, to that measured based on the video. We concluded that the resulting error in measuring the orifice area was approximately 20%, which also applies to the measurements with turbine flowmeters described below.

3.2. Turbine Flowmeters

The turbine flowmeter (TFM) design is similar to that of flowmeters used in pipe systems [e.g., *Munson et al.*, 2005]. The TFM principal components include (1) main body (flow tube), (2) turbine rotor assembly, and (3) upper and lower bearing supports (Figure 4). It also incorporates a handle and a pipe adapter (Figure 5a). We developed two versions of the turbine flowmeter, TFM1 and TFM2, which differ by their rotor assemblies. Otherwise, their designs are similar. We first describe TFM1 and then indicate how TFM2 differs from TFM1.

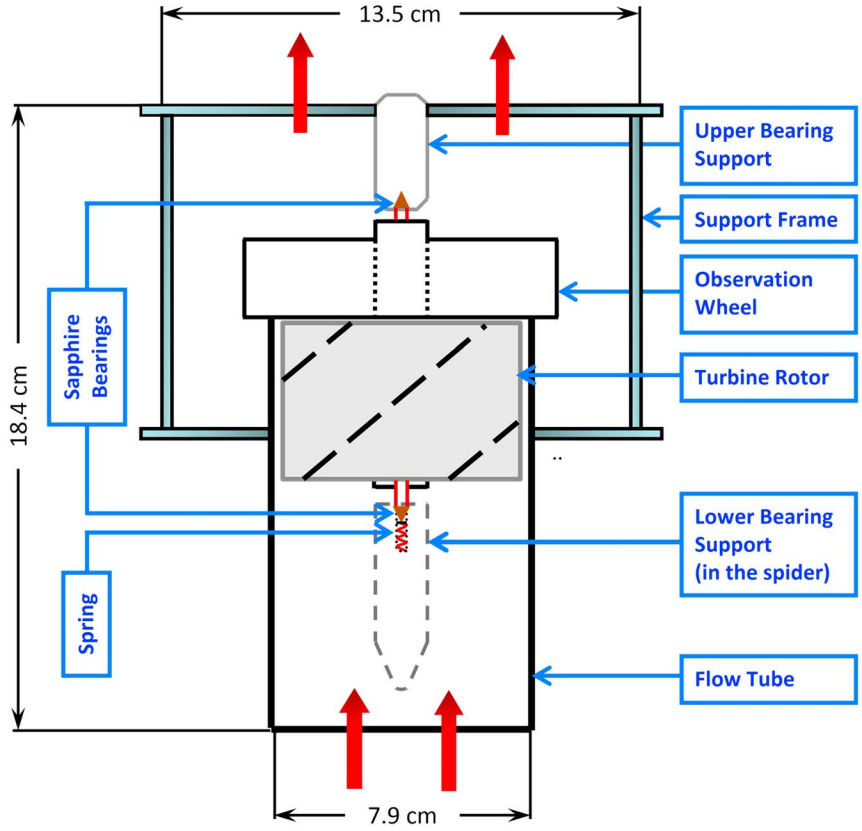

Figure 4. Schematic drawing (not to scale) of the turbine flowmeter showing the major design components. The internal diameter of the flow tube is 7.9 cm. The pipe adapter (Figure 5a) is not shown to simplify the drawing.

Most of the TFM1 components are made from molybdenum-alloyed austenitic stainless steel grade 316 [e.g., *ASTM*, 2010], which is the preferred grade of stainless steel for salt water exposure [*ASM*, 2005]. The main body (flow tube) has an internal diameter of 7.9 cm and houses the turbine rotor assembly, which consists of the turbine and an observation wheel (Figures 4 and 5). Since the rotor is covered by the flow tube walls and cannot be directly observed, the wheel protrudes outside the flow tube. This allows for visualizing the rotations from the submersible. The rotor assembly is concentrically mounted on the lower and upper bearings and is supported on both ends by sapphire jewels (Figure 6). The lower bearing is loaded by spring pressure. The spring pressure is adjustable and allows for optimal bearing preload, which enables smooth and consistent operation. For the sake of robust and reliable performance in the deep-sea environment, the instrument configuration does not include electronic sensors to collect and record the rotation rate. The modular design of the flowmeter does allow for efficient adaptation of electronic sensors, however.

When the instrument is placed over a vent orifice or diffuse flow site (Figure 7a), hydrothermal fluid flows through the rotor assembly. The device is held in place by a manipulator arm of the submersible, and the flow exerts a torque that initiates the rotation. A white mark is painted on the observation wheel of the rotor assembly as a reference (Figure 5a), so that rotations of the turbine rotor can be determined from video imagery recorded using standard *Alvin* or ROV video equipment. The rotation rate is converted to linear velocity using the calibration curves (section 4). Heat flux is then determined from equation (1).

Although we obtained a significant number of reliable measurements with TFM1 at flow velocities greater than 8 cm/s (section 6), we designed another turbine flowmeter device, TFM2, to determine lower flow velocities (Figures 7b). Support frames and flow tubes of TFM1 and TFM2 are identical, but we modified the configuration of the turbine rotor assembly. Because low flow velocities are more characteristic for diffuse flow, which is transparent or semitransparent, we removed the observation wheel to reduce the

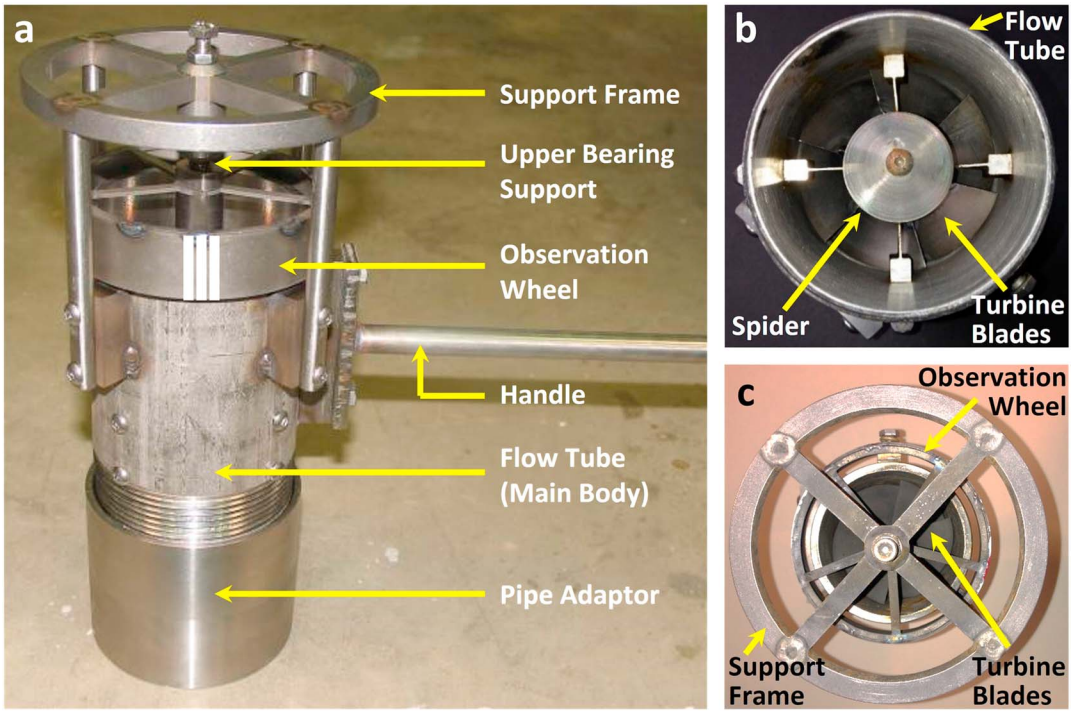

Figure 5. (a) Turbine flowmeter TFM1 and its (b) bottom (with pipe adaptor removed) and (c) top views.

turbine weight and fluid drag forces (compare Figures 7a and 7b). To further reduce its weight and to increase sensitivity, we used grade 2 titanium [*ASTM*, 2011] to manufacture the turbine rotor. We also changed the pitch angle (i.e., the angle of the blade inclination with respect to the rotor axis) from 45° in TFM1 to 65° in TFM2. The sensitivity of TFM2 can be further increased by using materials with lower friction on contacts, such as coated titanium versus synthetic sapphire, or employing more sophisticated blade geometry (e.g., helically twisted that generates larger rotating moments [*Baker*, 1993; *Merzkirch*, 2005]).

A deployed TFM2 is shown in Figure 7b. Note that we did not use the pipe adapter with TFM2, which reduced the distance between the diffuse flow source and the rotor assembly. We did use the adapter, however, with TFM1 during the measurements on black smokers. It protects the rotor from occasional chimney debris and allows the high-velocity flow to better approach the stable pattern before it enters the rotor zone. The calibration tests for TFM1 and TFM2 (section 4) were conducted with and without the pipe adapter, respectively.

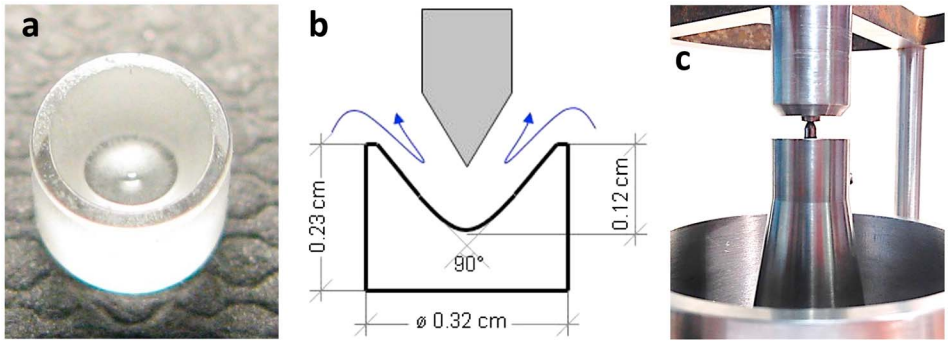

Figure 6. (a) Sapphire vee jewel, (b) schematics of sapphire jewel bearing support, and (c) TFM2 upper bearing support (identical to that of TMF1).

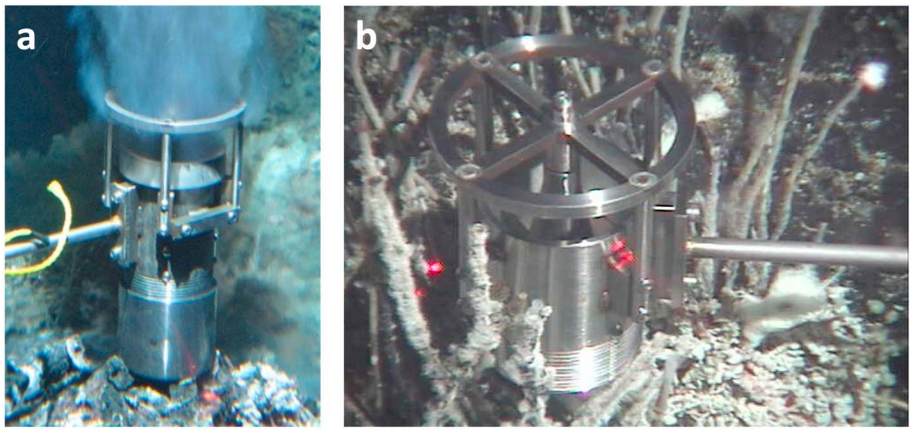

Figure 7. (a) Deployment of TFM1 at a black smoker on the Fairy Castle vent structure at the High Rise vent field (*Alvin* dive 4526). The fluid flow rate was 114.1 cm/s (measurement 18 in Table 3). (b) TFM2 deployed at a diffuse flow site at the Ventor vent structure in the High Rise vent field (*Alvin* dive 4620). Distance between two red laser beams, indicated by the red dots, is 10 cm (although in this case, the distance between the red dots is greater than that since the dots are not located on a plane perpendicular to the beams). The velocity of the diffuse fluid was 2.1 cm/s (measurement 25 in Table 3).

3.3. Comparison Between the Cup Anemometer and Turbine Flowmeters

Sea trials (section 6) showed that both devices performed successfully and required little (if any) postdive shipboard maintenance such as cleaning the components, repainting the observation mark or adjusting spring tension. Both the anemometer and turbine flowmeters incorporate an open sapphire jewel bearing system (Figure 6) that distinguishes these flowmeters from previously designed instruments [e.g., *Converse et al.*, 1984; *Ginster et al.*, 1994]. This key component in the design of the devices allowed hydrothermal fluid to simply flow pass the bearings (Figure 6b). As a result, particle precipitation and clogging on the critical parts of the device (i.e., sapphire bearings) was eliminated.

Due to the difference in axis orientation, the rotation of the TFM axis is much smoother and more consistent than for the cup anemometer. This difference is important for long-term deployment. The TFM has an axis orientation that is parallel to the flow direction. Therefore, the primary load on the bearings results from the axial (thrust) force component. The bearing preload is only required to maintain the axial alignment, as radial loads are minimal. Conversely, the anemometer axis is perpendicular to the fluid flow. This exerts a significant radial load on the sapphire jewels and rotating shaft. The ability to carry the radial load is dependent on the bearing preload. Consequently, the anemometer required higher preloads that contributed to higher friction and somewhat larger amounts of wear in the bearings.

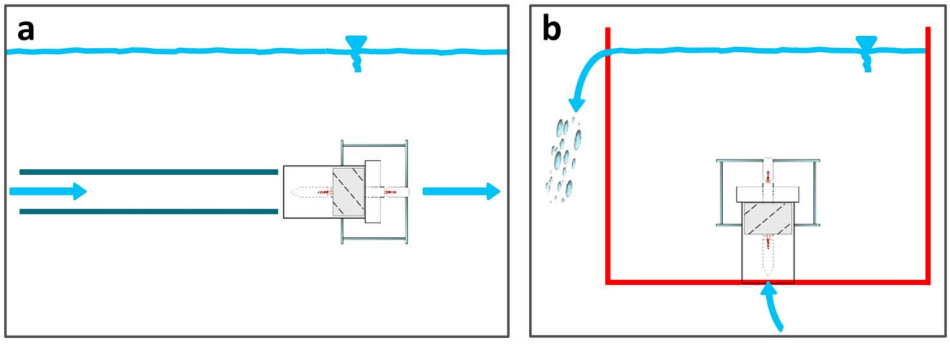

Figure 8. (a) Schematic of TFM1 calibration setup in the hydraulic flume. The rotations were simultaneously monitored by a stroboscope and a video camera. The number of revolutions corresponding to a certain flow rate was then determined postexperiment by using the recorded video imagery. The calibration curve shown in Figure 9a was constructed based on these measurements. (b) Schematic of the laboratory setup for calibrating TFM2 at low flow rates. Calibrations were performed in a container by changing the flow rates from the water faucet. The relatively slow rotations were videotaped, visually counted, and plotted on the calibration curve (Figure 9b) for velocities ranging from 2 to 10 cm/s.

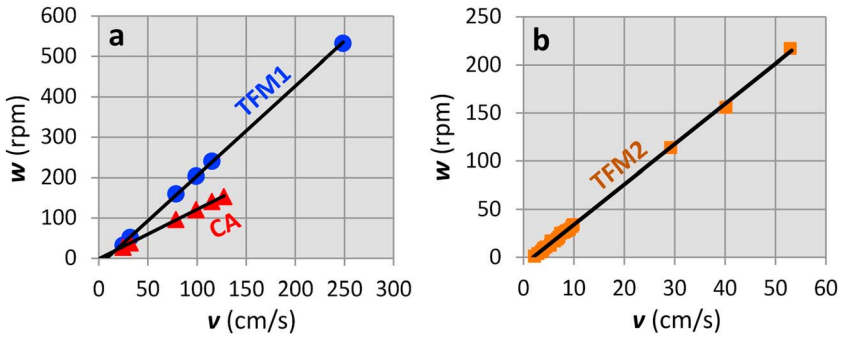

Figure 9. Calibration results for (a) the TFM1 device (circles) and cup anemometer (triangles) and (b) the TFM2 device (squares). The calibration lines shown are from postcruise calibrations. Precruise calibrations differ by less than 5% from the postcruise calibrations.

Occasionally, we replaced the sapphire jewels in the cup anemometer when they showed signs of wear or damage. Design of bearing supports allows their easy replacement. The TFM devices, however, did not require bearing replacement over the course of a cruise. Another advantage of the TFM devices is that the rotor assembly is contained inside the flow tube. This is a common configuration for flowmeters in conventional pipe systems [e.g., *Webster*, 1999]. Therefore, standard design approaches [*Merzkirch*, 2005; *Baker*, 2000] for blade geometry and pitch angle can be used for the configurations of TFM devices. Likewise, standard methods [e.g., *Baker*, 2000] can be employed for their calibration (section 4).

Our experience suggests that the TFMs are more robust instruments than the cup anemometer and are less likely to be damaged during transport or deployment by a submersible. Additionally, the closed-structure frame enables the TFM devices to completely sample the fluid jet by enclosing the flow (e.g., Figure 7a).

We note that enclosing the black smoker flow in the stainless steel flow tube of the TFM devices makes its hot internal surface more susceptible to aggressive particle precipitation. This effect can be minimized, however, by replacing the steel flow tube by a titanium one. This would be an effective solution for a long-term deployment of TFM devices.

When the venting fluid becomes saturated, minerals will precipitate to some degree on whatever surface is present. Titanium is frequently used in the seawater environment because it is generally less reactive than steel and shows little or no corrosion. It may not be possible to completely prevent mineral deposition as some nucleation spots may be available even on a very smooth titanium surface. Hence, in addition to using titanium, mineral deposition can be minimized during long-term deployments by minimizing entrainment of ambient seawater.

4. Calibration

4.1. Calibration Method

The cup anemometer and TFM1 were calibrated in the hydraulics lab of Georgia Tech before and after deployment. The calibration procedure consisted of a transparent flume and an injection pipe with a water source capable of constant and adjustable flow rates. The inner pipe diameter was 52.5 mm (≈5 cm), which represents a typical black smoker orifice. Calibrations were performed with a pipe located inside the flume to mimic the orifice of a vent chimney, and the devices were held near the opening of the pipe (Figure 8a). To evaluate the performance of TFM1 and the cup anemometer at flow rates characteristic of focused hydrothermal venting [e.g., *Ramondenc et al.*, 2006], we calibrated both devices at flow velocities of 25 to 249 cm/s and 27 to 141 cm/s, respectively (Figure 9a). Rotation rates were determined during the test by using a stroboscope [e.g., *van Veen*, 1977].

To calibrate TFM2 for flow velocities characteristic for diffuse hydrothermal flow [e.g., *Ramondenc et al.*, 2006; *Sarrazin et al.*, 2009], we used the experimental setup shown in Figure 8b. This setup included a plastic container used as a water reservoir. TFM2 was placed in the container by fitting its main body to the 5 cm hole drilled at the bottom of the container. Water was fed at a constant rate directly into the turbine and

Table 2. Flow Rate and Heat Output Measurements Performed With the Cup Anemometer Device at the Endeavour Segment and Axial Seamount on the JdF Ridge

Alvin Dive	Measurement Number	Depth (m)	Flow Regime	Flow Velocity (cm/s)	Temperature (°C)	Orifice Diameter (cm)	Source Area[a] (cm^2)	Flow Rate (cm^3/s)	Heat Output (kW)
				Main Endeavour Vent Field (Endeavour)					
Crypto (47°56.9797′N, 129°5.8191′W)									
4452	1	2,201	Focused	71.1	328.3	7	38.5	2,740	3,570
Dante (47°56.9527′N, 129°5.8793′W)									
4415	2	2,191	Focused	53.5	318.6	2.5	4.9	262	332
4421	3	2,197	Focused	12.5	201	3.6	10	130	100
4421	4	2,176	Focused	57.1	330[b]	8	50.3	2,870	3,770
4422	5	2,174	Focused	21.2	335.7	3	7.1	150	200
4422	6	2,175	Focused	6.2	333.3	4	12.6	78.1	104
4422	7	2,175	Focused	7.9	330[b]	2	3.1	24.5	32.1
4422	8	2,175	Focused	10.3	330[b]	1.5	1.8	18.5	24.3
4422	9	2,175	Focused	4.2	142	1	0.8	3.4	1.9
4422	10	2,175	Diffuse	10.2	312		12.6	129	159
4422	11	2,184	Focused	4.2	225	5.6	24.6	103	92
4422	12	2,185	Focused	24.5	328	8	50.3	1,230	1,610
4422	13	2,185	Focused	19.9	300.7	7	38.5	766	916
4422	14	2,182	Focused	65.8	333.1	4	12.6	829	1,100
4422	15	2,181	Focused	46.1	334.7	4	12.6	581	773
4422	16	2,186	Focused	8.5	251	1.2	1.1	9.4	9.3
4422	17	2,180	Focused	21.2	310	5	19.6	416	512
4439	18	2,176	Focused	26.7	327.5	8.3	54.1	1,440	1,880
4439	19	2,176	Focused	63.0	325	5	19.6	1,230	1,600
4441	20	2,185	Focused	45.1	328.9	7	38.5	1,740	2,270
4447	21	2,175	Focused	63.4	325.7	8.5	56.7	3,590	4,660
4447	22	2,175	Focused	59.0	322.9	6	28.3	1,670	2,140
4452	23	2,176	Focused	7.6	163	4	12.6	95.8	61.7
4452	24	2,176	Focused	24.1	249	3	7.1	171	169
Grotto (47°56.9473′N, 129°5.9114′W)									
4439	25	2,187	Focused	40.4	330[b]	7	38.5	1,560	2,040
4439	26	2,185	Focused	44.3	324	6	28.3	1,250	1,620
4439	27	2,189	Focused	35.0	330	6	28	980	1,290
4439	28	2,187	Focused	45.5	334	7.9	49	2,230	2,960
4441	29	2,200	Diffuse	4.2	20[b]		2,400	10,100	730
Hulk (47°57.0067′N, 129°5.8272′W)									
4414	30	2,186	Focused	18.4	322	7	38.5	708	907
4414	31	2,186	Focused	45.1	322	7	38.5	1,740	2,220
4414	32	2,187	Focused	46.0	313	3.9	11.9	550	680
4414	33	2,186	Focused	17.4	312	8	50.3	875	1,090
4414	34	2,192	Focused	72.1	320.3	5.6	25	1,800	2,300
4416	35	2,193	Focused	20.0	146	8	50.3	1,010	580
4416	36	2,192	Focused	12.1	321.1	8.5	56.7	686	876
4416	37	2,192	Diffuse	11.5	257		19.6	225	230
4416	38	2,184	Focused	16.7	278.4	2.7	5.7	95.2	105
4416	39	2,188	Diffuse	17.5	272.4		95	1,660	1,800
4416	40	2,188	Focused	28.3	279	6	28.3	801	888
4416	41	2,189	Diffuse	12.4	304.3		50.3	624	754
4420	42	2,186	Focused	20.6	160	4	12.6	260	160
4421	43	2,191	Focused	88.1	320	9	63.6	5,600	7,130
4447	44	2,189	Focused	11.1	309.3	5	19.6	218	268
4449	45	2,197	Focused	13.1	15.5	4.5	16	210	11
4452	46	2,192	Focused	53.8	327.7	3.5	9.6	516	673
4452	47	2,191	Focused	14.6	85.1	4	12.6	184	61.2
4452	48	2,188	Focused	28.8	320.1	4	12.6	363	462
S&M 2008 (47°56.8718′N, 129°5.9194′W)									
4446	49	2,189	Diffuse	12.1	20[b]		78.5	950	68.8
TP (47°56.9716′N, 129°5.8593′W)									
4420	50	2,194	Focused	13.7	118.9	2	3.1	42.5	19.9
4447	51	2,174	Focused	4.2	337.3	5	19.6	82.3	110

Table 2. (continued)

Alvin Dive	Measurement Number	Depth (m)	Flow Regime	Flow Velocity (cm/s)	Temperature (°C)	Orifice Diameter (cm)	Source Area[a] (cm^2)	Flow Rate (cm^3/s)	Heat Output (kW)
4447	52	2,173	Focused	61.6	330[b]	6	28.3	1,740	2,290
4447	53	2,174	Focused	16.7	330[b]	4	12.6	210	276
4452	54	2,191	Focused	82.6	333.7	3.7	10.8	892	1,180
					Mothra Vent Field (Endeavour)				
Faulty Towers (47°55.4202′N, 129°6.5372′W)									
4418	55	2,277	Focused	78.5	312.9	10	78.5	6,160	7,670
4418	56	2,277	Focused	58.9	314.9	12	113	6,660	8,300
4450	57[c]	2,271	Focused	82.5	321.3	13	133	11,000	14,000
4450	58	2,276	Focused	54.8	324	11	95.0	5,210	6,710
4450	59	2,171	Diffuse	9.6	107		177	1,700	714
Stonehenge (47°55.2666′N, 129°6.5814′W)									
4450	60	2,290	Focused	50.0	309.5	5	19.6	980	1,210
					Clam Bed Vent Field (Endeavour)				
(47°57.7837′N, 129°5.4822′W)									
4412	61	2,186	Diffuse	11.2	228		479	5,360	4,850
4412	62	2,187	Diffuse	11.5	277		133	1,530	1,680
					Axial Seamount				
Vixen (45°55.0338′N, 129°59.5881′W)									
4444	63	1,521	Focused	44.1	333	5.3	22.1	975	1,290
Diva (45°55.5784′N, 129°58.7485′W)									
4445	64	1,522	Focused	13.1	280[b]	5.5	24	310	350

[a]Source area for diffuse flow estimated by bio prominence.
[b]Temperature is inferred from additional measurements at the same vent.
[c]Hot Harold vent.

filled the container. Once the container was filled, the water level was kept constant by allowing water to flow out freely through a hole drilled on the upper wall of the container (Figure 8b). The number of full rotations completed by the rotor per unit time was counted visually and recorded. This process was repeated for flow velocities between 2 and 10 cm/s (Figure 9b).

Although TFM2 was designed to be used primarily at diffuse flow sites, we also calibrated it at higher velocities, up to 53 cm/s (Figure 9b), for use in focused transparent and semitransparent flows, such as white and gray smokers. This calibration was done in the same flume as that for TFM1 and the cup anemometer. Calibrations in both laboratory setups (Figure 8) resulted in the same calibration line (Figure 9b).

4.2. Calibration Results

The results of the calibration tests are plotted in Figure 9 and are fit with linear dependence

$$w = w_0\left(\frac{v}{v_0} - 1\right) \tag{2}$$

where w is the number of rotations per unit time and v is the linear flow velocity. The fitting parameters are $w_0 = 1.710$ rpm and $v_0 = 1.389$ cm/s for the cup anemometer, $w_0 = 18.326$ rpm and $v_0 = 8.238$ cm/s for TFM1, and $w_0 = 8.192$ rpm and $v_0 = 1.953$ cm/s for TFM2. The values of the coefficient of correlation, r^2, are all greater than 0.98. Quantity v_0 represents the minimum velocity required to overcome and initiate rotations. For all calibrations, $v_0 > 0$ and $w_0 > 0$.

In some instances, measurement results (in Tables 2–4) are extrapolated beyond the calibration range of the flowmeters (Figure 9), which is acceptable due to the linear calibration curves (Figure 9). In instances of very low discharge during field tests, only unsteady, quasiperiodic rotations occurred, indicating that flow through the meters was not sufficiently strong to rotate the meter blades continuously. In this case, using equation (2) (or its inverse) yields the lower limit of flow velocity that corresponds to the measured time-averaged rotation rate. In such cases, the results should be viewed as lower estimates of flow rates. These estimates, however, are probably quite close to the actual discharge rates (section 5.1).

Table 3. Flow Rate and Heat Output Measurements Performed With the TFM1 and TFM2 Devices at the Endeavour Segment, Axial Seamount, and Middle Valley on the JdF Ridge

Alvin Dive	Measurement Number	Depth (m)	Device	Flow Regime	Flow Velocity (cm/s)	Temperature (°C)	Orifice Diameter (cm)	Source Area[a] (cm^2)	Flow Rate (cm^3/s)	Heat Output (kW)
					Main Endeavour Vent Field (Endeavour)					
Dante (47°56.9527′N, 129°5.8793′W)										
4518	1[b]	2,179	TFM1	Focused	84.0	336	4.5	15.9	1,340	1,780
4518	2	2,194	TFM1	Diffuse	13.1	12		7,100	93,000	3,760
4525	3[b]	2,179	TFM1	Focused	92.0	338	4.5	15.9	1,460	1,970
4526	4	2,181	TFM1	Focused	98.8	327	7.9	49.0	4,840	6,300
Grotto (47°56.9473′N, 129°5.9114′W)										
4621	5	2,188	TFM1	Focused	40.1	290	3.4	9.1	365	421
4622	6	2,188	TFM2	Diffuse	2.0	13.9		1,090	2,180	105
4626	7	2,186	TFM1	Focused	134.0	320	7.9	49.0	6,570	8,400
4627	8	2,190	TFM2	Diffuse	5.9	20		1,580	9,320	675
4627	9	2,188	TFM2	Focused	2.0	20.3	2	3.1	6.2	0.5
4627	10	2,188	TFM2	Diffuse	12.7	42.6		50	635	103
Hulk (47°57.0067′N, 129°5.8272′W)										
4627	11	2,193	TFM2	Diffuse	2.1	15.9		1,770	3,720	208
4627	12	2,193	TFM2	Diffuse	9.8	14.8		4,530	44,400	2,290
4626	13	2,199	TFM1	Focused	51.1	306	4.1	13.2	675	820
4626	14	2,192	TFM1	Focused	151.3	310	7.8	47.8	7,200	8,900
					Mothra Vent Field (Endeavour)					
Faulty Towers (47°55.4202′N, 129°6.5372′W)										
4628	15	2,278	TFM1	Focused	76.1	318	9	63.6	4,840	6,120
					High Rise Vent Field (Endeavour)					
Bambi (47′58.1173′N, 129′5.2181′W)										
4623	16	2,140	TFM1	Focused	155.1	337	8	50.3	7,800	10,460
Boardwalk (47°58.1075′N, 129°5.2294′W)										
4623	17	2,134	TFM1	Focused	59.5	324	5.2	21.2	1,260	1,630
Fairy Castle (47°58.0266′N, 129°5.2896′W)										
4526	18	2,158	TFM1	Focused	114.1	329	5	19.6	2,240	2,930
Godzilla (47°58.1183′N, 129°5.2415′W)										
4516	19	2,136	TFM1	Focused	198.6	349	10	78.5	15,600	21,600
Park Place (47°58.0913′N, 129°5.2695′W)										
4516	20	2,149	TFM1	Focused	57.4	315	4.2	13.9	798	999
4623	21	2,148	TFM1	Focused	31.2	250	4	12.6	393	390
Ventor (47°58.0589′N, 129°5.3779′W)										
4516	22	2,164	TFM1	Focused	138.4	332	3	7.1	983	1,300
4526	23	2,163	TFM1	Focused	135.2	333	4.5	15.9	2,150	2,850
					Axial Seamount					
Marker 134 (45°56.1538′N, 129°58.8917′W)										
4620	24	1,517	TFM2	Diffuse	2.1	5		1,210	2,540	31.5
4620	25	1,517	TFM2	Diffuse	2.1	4.8		1,510	3,170	36.8
Marker 33/55 (45°55.9871′N, 129°58.9472′W)										
4521	26	1,520	TFM2	Diffuse	4.1	19.6		49	201	14.2
					Dead Dog Vent Field (Middle Valley)					
Dead Dog Mound (48°27.3635′N, 128°42.5814′W)										
4625	27	2,406	TFM1	Focused	171.6	260	12	113	19,400	20,000
4625	28	2,399	TFM1	Focused	186.3	265	11	95	17,700	18,600

[a]Source area for diffuse flow estimated by bio prominence.
[b]Measurements during *Alvin* dives 4518 and 4525 conducted on the same orifice.

5. Accuracy of Measurements

Accuracy of our measurements is affected by two main sources of error: (1) mechanical characteristics of the flowmeters and (2) uncertainties associated with field conditions. Some inaccuracies of flowmeters are typical even for ideal laboratory conditions, whereas others are specific for our designs and applications.

Table 4. Flow Rate and Heat Output Measurements Performed With the TFM1 and TFM2 Devices at 9°50′N on the East Pacific Rise

Jason Dive	Measurement Number	Depth (m)	Device	Flow Regime	Flow Velocity (cm/s)	Temperature (°C)	Orifice Diameter (cm)	Source Area[a] (cm^2)	Flow Rate (cm^3/s)	Heat Output (kW)
					East Pacific Rise					
P-vent (9°50.2720′N, 104°17.4640′W)										
758	1	2,509	TFM2	Diffuse	3.7	8.6		9,630	35,600	950
758	2	2,511	TFM1	Focused	45.0	284	1.5	1.8	81.0	91.4
758	3	2,499	TFM1	Focused	24.6	272.4	5	19.6	482	522
758	4	2,499	TFM1	Focused	21.0	165	5	19.6	412	269
Crab Spa (9°50.3975′N, 104°17.4883′W)										
758	5[b]	2,502	TFM2	Diffuse	9.8	16		314	3,080	174
758	6	2,502	TFM2	Diffuse	3.9	8.8		314	1,220	33.8
758	7[b]	2,502	TFM2	Focused	12.0	22.4	3.1	7.5	90.0	7.4
758	8[b]	2,502	TFM2	Diffuse	6.1	20.6		306	1,870	140
M-vent (9°50.7997′N, 104°17.5913′W)										
759	9	2,498	TFM2	Focused	2.8	24.2	1.5	1.8	5.0	0.4
Bio 9 (9°50.3056′N, 104°17.4764′W)										
760	10	2,505	TFM1	Focused	101.1	363	2.4	4.5	450	700
Tica (9°50.3981′N, 104°17.4927′W)										
758	11	2,511	TFM2	Diffuse	17.2	167		1,400	24,100	15,900
Colonizer CV61 (9°50.2766′N, 104°17.4718′W)										
758	12	2,506	TFM2	Focused	12.3	77.9	2.5	4.9	60.3	18.3

[a]Source area for diffuse flow estimated by bio prominence.
[b]Measurements done at the same site. The flow appeared diffuse (measurement 5) before the organisms occupying the site were removed. After removal, a flow source (small fracture) was exposed (measurement 7), although a significant component of the diffuse flow (measurement 8) remained.

5.1. Flowmeter Performance

Flowmeter performance is often characterized by the flowmeter factor $K = w/Q$ [e.g., *Hochreiter*, 1958; *Webster*, 1999], where Q is the flow rate and w is the frequency of rotation. For flow measurements in pipe systems, it is desirable to use a flowmeter within its "linear" range, where K is approximately constant [e.g., *Baker*, 1993, 2000]. Once the frequency of rotations is measured, the flow rate is simply obtained from $Q = w/K$. Typical

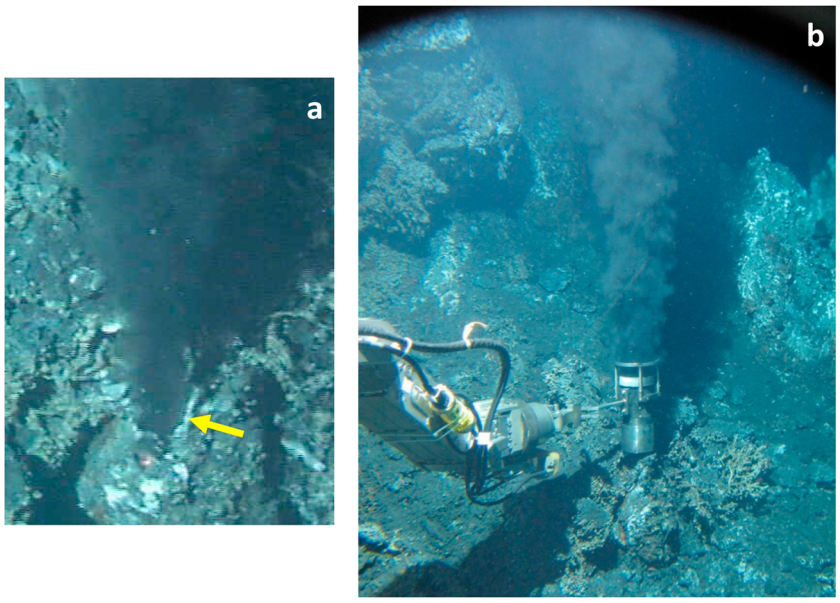

Figure 10. (a) Focused flow (orifice denoted by the arrow) at the Dante structure (MEF, *Alvin* dive 4518) located at $X = 4999$ m, $Y = 6135$ m (47°56.9446′N, 129°5.8591′W), at the depth of $Z = 2179$ m. No reliable in-hull, long-baseline (LBL) navigation was achieved during dive 4518, so these local *Alvin* coordinates are the Doppler fixes with several surface LBL and USBL corrections applied during the dive. (b) TFM1 device deployed at this black smoker. The measured flow velocity was 84.0 cm/s (measurement 1 in Table 3).

flowmeter design criteria require K to be approximately constant for flow rates in the range of $0.1Q_{max}$ to Q_{max}, where Q_{max} is the maximum expected flow rate [e.g., *Webster*, 1999; *Baker*, 2000]. The K factor is specific for given fluid properties. For our flowmeters, the calibration curves in Figure 9 show a strong linear relationship between w and v (or equivalently Q), suggesting that these devices are operating within standard design specifications for such flowmeters.

An important factor associated with field conditions that may lead to inaccuracy of velocity measurements is the temperature difference between the lab calibration and field conditions. At elevated temperatures, the meter material undergoes thermal expansion, which may result in deformation of its components. Temperature variations have not compromised the structural stability of our devices during sea trials (section 6). In industrial applications, flowmeters made of the same or similar materials operate at temperatures varying from −270°C [*Grey*, 1960] to 650°C [*Webster*, 1999] and pressures ranging from nearly a vacuum to those exceeding 400 MPa [*Webster*, 1999]. It is probably more important for black smoker measurements that the density of hot hydrothermal fluid is approximately 40% lower than that of the room temperature water we used in our calibration tests (section 4.1). This may result in as much as a 15% error [*Baker*, 1993]. The high temperature of black smokers also yields lower kinematic viscosity. Its effect on the accuracy of the flow measurements may result in an error of the same order as the density effect. For example, in experiments conducted by *Cuthbert and Beck* [1999], an order-of-magnitude change of the liquid viscosity resulted in the change of K of approximately 10%.

Therefore, even when the field conditions are significantly different than the calibration conditions, we estimate that the overall error in measured velocity does not exceed 30% at black smokers. The error in the measurement of diffuse flow velocity is likely to be considerably smaller. Compared to flowmetering in industrial pipes, where the attainable measurement error could be as low as 0.1% [e.g., *Webster*, 1999; *Baker*, 2000], the level of accuracy in our devices may appear to be relatively low. This level of accuracy is acceptable in the seafloor hydrothermal environment, however, because assumptions regarding conditions in the field may be more problematic than inaccuracies resulting from the flowmeters themselves. Fluid flow rates likely vary with time over tidal cycles and as a result of changes in bottom currents. Our flowmeters could capture these variations or obtain long-term mean flow rates if they are deployed for longer periods of time.

5.2. Entrainment of Ambient Seawater

It is important to contain the flow within the measuring device as much as possible to minimize entrainment. High-temperature hydrothermal fluid is essentially transparent as it exits the vent orifice, but it attains its black color almost immediately when it mixes with the ambient seawater and minerals begin to precipitate. The fact that the flow can be clearly seen (Figures 7a and 10) as a result of mineral precipitation indicates at least some entrainment of ambient seawater. When using the flowmeter devices, we measure temperature at or within the orifice, but the flow velocity is measured several centimeters above the orifice. As a result of entrainment, the flow velocity may be either increased or decreased somewhat from the velocity at the orifice [e.g., *Morton and Middleton*, 1973; *van den Bremer and Hunt*, 2010]. This results in an overestimation or underestimation, respectively, of the actual flow rate at the orifice.

The uncertainty of measurements associated with entrainment is also common in other direct methods of measuring advective heat flow at the vent scale. In particular, the entrainment assumption used in turbulent plume models can significantly affect results of flow measurements. For example, *Carazzo et al.* [2008] conclude that the heat flux from a hydrothermal plume on the TAG mound is 3 times greater than that obtained by *Rudnicki and Elderfield* [1992], who used the same data set as *Carazzo et al.* [2008], but with a different entrainment coefficient.

To assess the effect of entrainment uncertainty on the accuracy of measurements, we consider the data obtained for a black smoker at Dante shown in Figure 10. For this example, our measurements showed (Table 3, measurement 1 *Alvin* dive 4518) that hydrothermal fluid of temperature $T = 336$°C enters ambient seawater of temperature $T_a = 1.9$°C through the orifice of diameter $2b_0 = 4.5$ cm with the mean flow velocity of $V_0 = 84$ cm/s. The corresponding Reynolds number $Re = 2b_0\rho_0 V_0/\eta_0 \approx 2.5 \times 10^5$, where the fluid density $\rho_0 \approx 650$ kg/m^3 and viscosity $\eta_0 \approx 10^{-4}$ Pa s at $T_0 = 336$°C and pressure $P \approx 21$ MPa, which corresponds to the water depth of 2179 m at the measurement site. Because in jet and plume flows, turbulence develops at $Re = 2000$–4000 [e.g., *Fischer et al.*, 1979], $Re \sim 10^5$ indicates turbulent flow. Turbulence is typical for all other measurements we made for the focused venting (Tables 1–4).

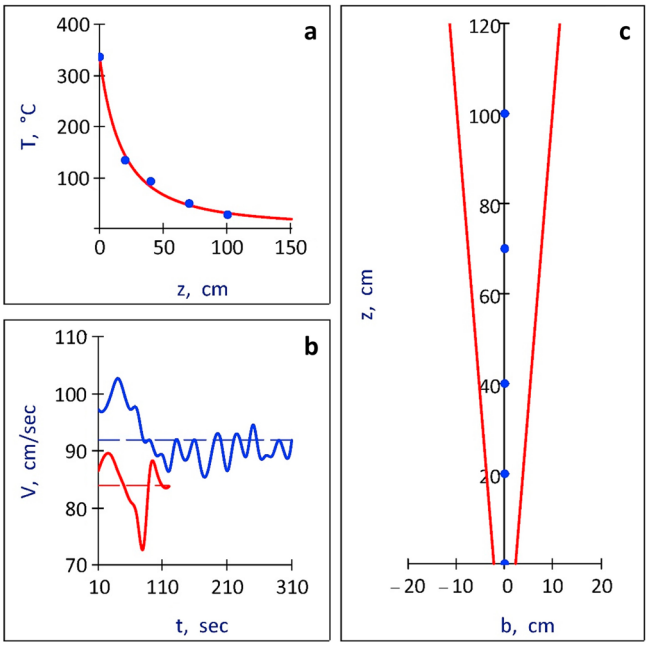

Figure 11. (a) The best fit of the temperature values (blue points) to the turbulent plume model (bold red line) (L. N. Germanovich et al., submitted manuscript, 2015). The mean flow temperatures $T = (T_c + T_a)/2 = 133.9$, 92.4, 48.9, and 31.9°C were used for all but the orifice measurement, where the actually measured value of $T_0 = 336$°C was used. Relation $T = (T_c + T_a)/2$ accounts for the difference between the measured centerline plume temperature, T_c, and the top-hat profile temperature, T. The measured flow velocity of $V_0 = 84.0$ cm/s (Table 3, measurement 1) represents the mean velocity across the orifice. The fit was obtained with only one matching parameter, the entrainment coefficient $\alpha = 0.064$. (b) Plume profile computed for $V_0 = 84.0$ cm/s and $\alpha = 0.064$. This profile resembles the plume in Figure 10b. (c) Velocity-time dependence measured with TFM1 at the orifice of a black smoker vent (Figure 10b) during *Alvin* dives 4518 and 4525 (red and blue lines, respectively). The shown velocity is averaged over the time window of 10 s. Red and blue dashed lines show the time-averaged velocities $V_0 = 84.0$ cm/s and $V_0 = 92.0$ cm/s, respectively (measurements 1 and 3 in Table 3).

We use the classic turbulent plume model [*Morton et al.*, 1956; *Morton*, 1959; *Morton and Middleton*, 1973; *Hunt and Kaye*, 2005; *Michauxa and Vauquelin*, 2008; *Hunt and van den Bremer*, 2011; *Candelier and Vauquelin*, 2012] and consider constant, time-averaged vertical velocity, $V(z)$, in each horizontal cross section inside the vertical plume while the ambient flow velocity outside the plume is zero. We also consider constant densities $\rho(z)$ and ρ_a (or temperatures $T(z)$ and T_a) inside and outside the plume, which has the radius of $b(z)$ in each horizontal cross section. Such velocity-density distributions are called "top-hat" profiles and correspond to the equivalent plume that possess the same mass, momentum, and buoyancy fluxes in each vertical cross section as the real flow. The plume source has the finite diameter $2b_0$. At the elevation, z, above the orifice,

$$V(z) = \frac{m(z)V_0}{q(z)} \tag{3}$$

where the scaled momentum, $m(z) = V^2b^2/(V_0^2b_0^2)$, and volume, $q(z) = Vb^2/(V_0b_0^2)$, fluxes in the plume are defined by [e.g., *Hunt and Kaye*, 2001; *van den Bremer and Hunt*, 2010]

$$m = \left(1 - \Gamma + \Gamma q^2\right)^{2/5},$$
$$2\alpha\frac{z}{b_0} = \int_1^q \left(1 - \Gamma + \Gamma x^2\right)^{-1/5} dx \tag{4}$$

Plume radius changes with height z above the orifice as

$$b(z) = \frac{q(z)b_0}{\sqrt{m(z)}} \tag{5}$$

In equation (4), the dimensionless parameter

$$\Gamma = \frac{5(\rho_0 - \rho_a)b_0}{8\alpha V_0^2\rho_a} \tag{6}$$

characterizes the plume type (pure jet, buyout jet or forced plume, pure plume, and lazy plume for $\Gamma = 0$, $1 < \Gamma < 0$, $\Gamma = 1$, and $\Gamma > 1$, respectively), $\rho_a \approx 1000$ kg/m^3 is the density of the ambient seawater, and α is Taylor's entrainment coefficient.

To evaluate α, L. N. Germanovich et al. (submitted manuscript, 2015) used *Alvin's* probe to measure the temperature distribution along a black smoker plume during *Alvin* dive 4518 (Table 3). They determined $\alpha = 0.064$ by fitting dependence [e.g., *Hunt and Kaye*, 2001]

$$T(z) = T_a + \frac{T_0 - T_a}{q(z)} \tag{7}$$

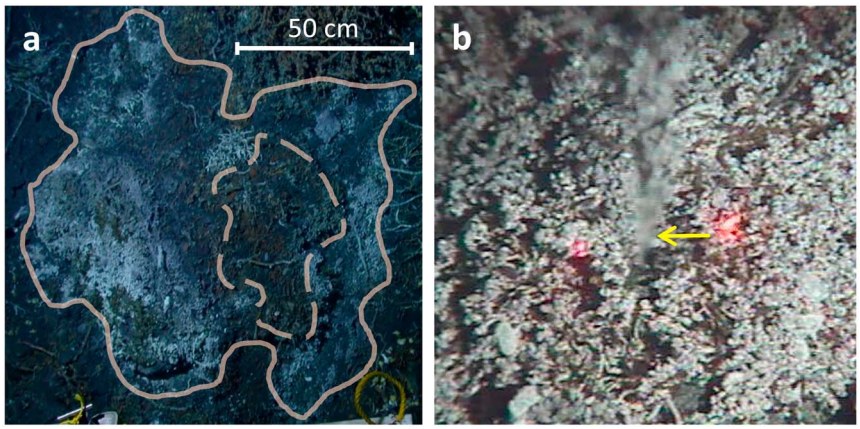

Figure 12. (a) Diffuse flow site near Dante structure (MEF, *Alvin* dive 4518) at $X = 5005$ m, $Y = 6168$ m (47°56.9527′N, 129°5.8793′W), and $Z = 2194$ m. TFM1 measured a flow velocity of 13.1 cm/s (measurement 2 in Table 3). White microbial mats visualize the area of diffuse venting, which is between the solid and dashed lines indicating its outer and inner borders, respectively. The shimmering water was distinctly observed above this area and was not visible outside, where no live biological activity could be detected. The area, 7100 cm^2, of this diffuse venting site was used in equation (1). We carefully analyzed this site, and it is unlikely that any measurable diffuse flow is venting from the area inside the dashed perimeter, but it cannot be entirely excluded. If this area were included in the calculation, the final result would differ by approximately 50%. (b) Vertical, low-temperature focused flow (indicated by arrow) within a diffuse flow site at $X = 4954$ m, $Y = 6153$ m (47°56.9543′N, 129°5.8952′W), and $Z = 2188$ m (Grotto, MEF, *Alvin* dive 4627). The source area of focused flow is defined by the orifice circumference while the source area of diffuse flow is estimated by bio prominence. TFM2 measured a flow velocity of 2.0 cm/s (measurement 9 in Table 3).

to these temperature measurements (Figure 11a). Here we used equations (3)–(6) to evaluate $V(z)$ and $b(z)$ (Figure 11b), the flow velocity, and plume radius respectively, along the plume axis, $z \geq 0$. Because the flowmeter location could have been uncertain by up to 5 cm in elevation, we computed the flow rate $V(0) = 90.2$ cm/s at the orifice, $z = 0$, which would correspond to velocity $V_0 = 84$ cm/s if it were measured at the height of $z_0 = 5$ cm above the orifice. Therefore, using the velocity measured by the TFM devices to calculate the volume flow and heat flux may result in an underestimate of approximately 7%. As discussed below, this error is relatively small compared to errors that may arise from the uncertainty in flow area and is of the order of transient flow rate fluctuations at the measurement timescale (section 5.4).

It is interesting to note that the representative value of the Taylor's entrainment coefficient reported in the literature is $\alpha \approx 0.12$ [e.g., *Morton et al.*, 1956; *Fischer et al.*, 1979; *Turner*, 1986; *Liedtke and Schatzmann*, 1997; *Bemis et al.*, 2002; *Rona et al.*, 2002; *Kaminsky et al.*, 2005]. The value of $\alpha = 0.064$ computed from our measurements (Figure 11b) is considerably smaller and may be representative near the source (of the order of meters) of the focused high-temperature hydrothermal flow in the deep ocean floor conditions (L. N. Germanovich et al., submitted manuscript, 2015). We note that using $\alpha = 0.12$ instead of $\alpha = 0.064$ increases the error in determining the flow rate and heat flux from 7% to approximately 20%, which is still acceptable.

Equations (3)–(6) are based on the Boussinesq approximation, which accounts for the density difference only in the buoyancy terms and means, in effect, that mass fluxes are equivalent to the volume fluxes in the plume [e.g., *Caulfield and Woods*, 1995]. Near the source region, where the Boussinesq assumption may not be valid, the high-density contrast between the hot hydrothermal fluid and cold ambient seawater may increase the rate of entrainment. If the plume is not Boussinesq already at the source, it approaches the Boussinesq limit as it rises because the density contrast is diluted by the entrained seawater. We found that differences between the flow velocities obtained using the Boussinesq and non-Boussinesq assumptions [e.g., *Rooney and Linden*, 1996; *Woods*, 1997; *Fannelop and Webber*, 2003; *van den Bremer and Hunt*, 2010] for plumes with a source of typical size do not exceed 10%. This indicates that for the black smoker shown in Figure 10, the flow can be considered essentially Boussinesq.

5.3. Field Conditions

Difficulties of working on the seafloor also affect measurement accuracy. Currently, the sampling of black smoker vents on large vent structures and throughout the vent field is incomplete, and to obtain

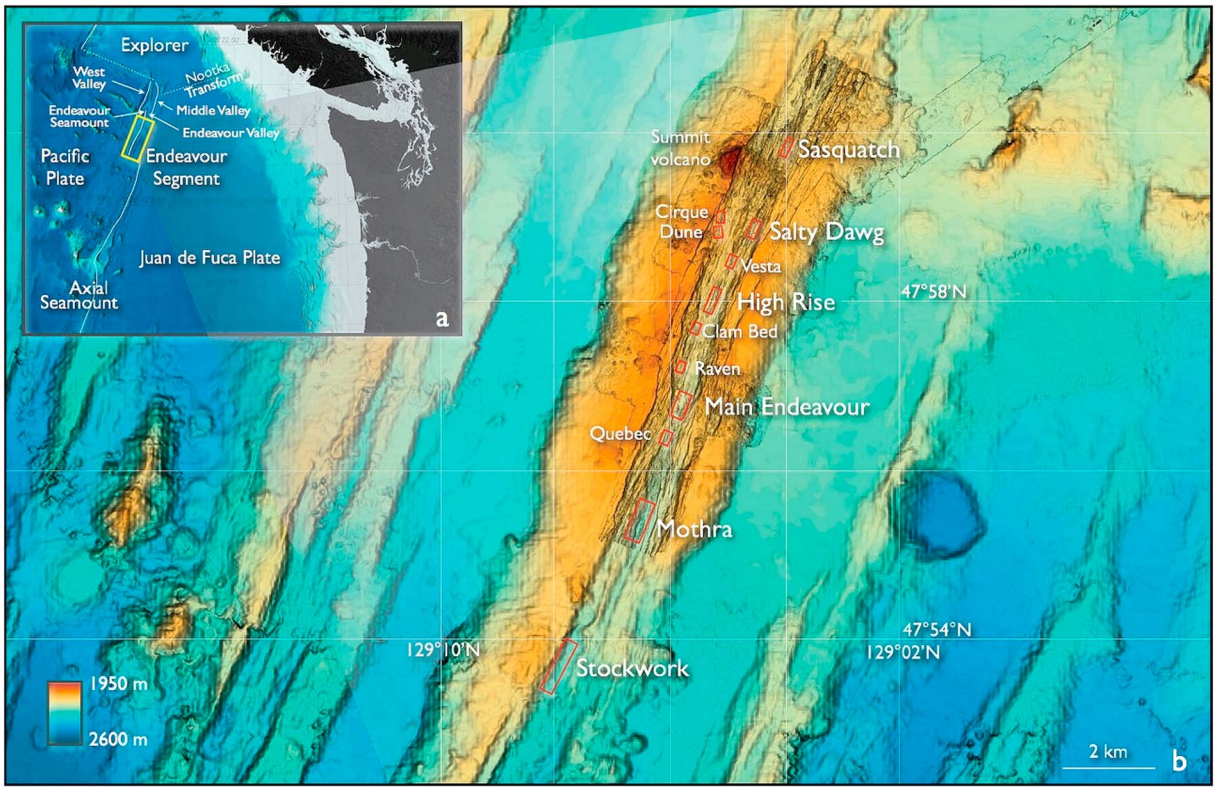

Figure 13. (a) Locations of the Endeavour segment, Axial Seamount, and Middle Valley [*Kelley et al.,* 2012] on the JdF Ridge. (b) Bathymetry map of the Endeavour segment showing hydrothermal vent fields [*Kelley et al.,* 2012].

estimates of heat flow on the vent structure or vent field scale requires extrapolation of the limited data set. Black smoker velocities are translated to volumetric flow rates by assuming circular orifices and somewhat inaccurate estimates of orifice area. Our estimate of the corresponding uncertainty is approximately 20% (section 3.1), whereas *Ginster et al.* [1994] assumed an uncertainty of ±5%. *Tivey and Singh* [1997] used X-ray computer tomography to study the morphology of the flow channels in black smoker chimneys. Their results suggest that orifice areas calculated assuming a circular geometry could be underestimated by 32% (on average by 16%; see Figure 2a in their work). All of these issues result in an estimate of black smoker heat outputs that are likely accurate to within ±50%.

Diffuse flow measurements have some of the same issues, but inaccurate assessment of the flow area of a diffuse flow patch and extrapolation to diffuse patches where measurements have not been made are likely the greatest sources of error in determining heat output. Figure 12a shows how we assess the area of a diffuse flow patch and suggests that the estimates could differ by up to 50%. As a result, heat output estimates using these devices are uncertain by roughly a factor of 2. Such uncertainties are similar to those estimated for both integrated and plume measurements [*Baker*, 2007].

During cup anemometer measurements, another source of error can come from cross flow that distorts the flow of the plume passing the anemometer wheel. Hence, the anemometer needs to be properly oriented to minimize this effect (Figure 3c). Measurements with the TFM devices are not significantly affected by such cross flow because the hydrothermal flow is mostly contained within the device (Figures 7a and 10b).

Determining the true velocity of the fluid exiting the chimney is not trivial. Given the assumptions required in designing and implementing the device, these measurements can be considered to be within approximately 20% of the true vent velocity (see section 5.2). Heat output data are likely to be uncertain by approximately a factor of 2, when extrapolated to the vent field scale. The data presented in this work are important, however, in that a wide range of velocities is presented. These variations in relative velocities highlight the complex flow conditions at vent fields.

5.4. Temporal Variability

Natural temporal variability of hydrothermal flow represents another source of inaccuracy if the measurement goal is the time-averaged fluxes. Table 3, dives 4518 and 4525, shows that repeat TFM1 measurements at the same location at Dante a week apart resulted in variance of heat flux of ≈10%, indicating that the device has a reasonably good degree of precision. Another example is given in Figure 11c, where the measured flow velocities are plotted during the time interval of several minutes. This example shows that the transient flow rate fluctuations within a few minutes can be as large as ≈15%, which is consistent with data in Table 1 in *Ramondenc et al.* [2006].

6. Sea Trials

The cup anemometer and turbine flowmeters were tested during five oceanographic expeditions from 2008 to 2014. The cup anemometer was deployed on eight *Alvin* dives on cruise AT15-34 to the Endeavour segment of JdF in 2008. On this cruise, a total of 35 measurements of fluid flow were obtained at vent structures in the MEF, Mothra field, and Clam Bed vent field (Figure 13). An additional 29 flow rate measurements were obtained during nine *Alvin* dives on cruise AT15-36 at the MEF, Mothra vent field, and Axial Seamount (Figure 13). Results of measurements with the cup anemometer device are given in Table 2. Most of the measurements were made at high-temperature vents as this device is more suitable for relatively high flow rates (Table 2).

TFM1 was tested during four *Alvin* dives on cruise AT15-47 to JdF in 2009, where a total of nine focused and diffuse flow measurements were made at the MEF and the High Rise field, and five *Alvin* dives on cruise AT15-67 to JdF in 2010, where a total of ten focused and diffuse flow measurements were made at Endeavour (MEF, Mothra, and High Rise field) and Middle Valley (Dead Dog field). One diffuse flow measurement was taken at the Axial Seamount on an *Alvin* dive during cruise AT15-47 using TFM2. TFM2 was also deployed on three *Alvin* dives during cruise AT15-67 when eight flow measurements were conducted at MEF and Axial Seamount. The devices were further tested in 2014 during three *Jason* dives on cruise AT26-10 to the East Pacific Rise (9°50′N) where four and eight measurements were taken using TFM1 and TFM2, respectively. Results obtained with TFM1 and TFM2 are given in Tables 3 and 4.

Locations of measurements reported in Tables 1–4 were originally recorded in the local *Alvin* coordinate set *X* (south-north) and *Y* (west-east). All measurements were conducted in the Universal Transverse Mercator (UTM) zone 9 [e.g., *Snyder*, 1997]. The local *X* and *Y* are the geodetic easting and northing adjusted by applying a false easting and false northing, respectively, to the standard UTM zone 9 projection based on the WGS84 datum [e.g., *Grafarend and Krumm*, 2006]. False easting and false northing for 2008, 2009, and 2010 cruises were the same, which resulted in the same local origins for these years. For dives at the Endeavour segment, the local origin is at 47.89390°N, 129.16450°W, at the Axial Seamount at 45.90000°N, 130.06670°W, and at Middle Valley at 48.41667°N, 128.73333°W. The local origin of measurements is at 9.13330°N, 104.33330°W (UTM zone 13) for the EPR 9°50′ and 9°39.5′. At Lau Basin [e.g., *Tivey et al.*, 2012], the local origin is at 20.36670°S, 176.20000°W for the Tow Cam vent field and is at 20.83330°S, 176.26670°W for the Autonomous Benthic Explorer (ABE) vent field (both at UTM zone 1).

In general, locations of flow sources on the deep ocean hydrothermal structures often tend to be transient with venting being sealed (shut down) in some locations and reappearing in neighboring locations. Hence, it is likely that at least some flow sources registered in Tables 1–4 do not exist anymore. In addition, due to the navigational issues on some dives (e.g., Figure 7 caption), it was not possible to convert all recorded local coordinates to the geodetic coordinates. Therefore, in Tables 1–4 we present the geodetic coordinates of hydrothermal structures rather than those of individual vents. That the vents were indeed located on the structures as presented in Tables 1–4 were verified by markers that were available for all reported structures.

Each time the cup anemometer device returned to the ship, its components were carefully examined to insure that the integrity of the device was maintained and the device was cleaned prior to each dive, particularly, when recovered from black smoker areas. In a few of these cases, the surfaces of the cups were darkened by particle accumulation, so they were repainted with distinct colors or numbered for monitoring and data analysis purposes. The TFM devices were carefully inspected but did not require any maintenance during cruises.

On some dives, measuring fluid temperature with *Alvin's* temperature probe was not possible for reasons independent of our devices (e.g., malfunctions of *Alvin*'s temperature probe or recording system). We used temperature values obtained on the same structure during different dives, for estimating heat output in such cases. Some of the data from both the cup anemometer and turbine flowmeters have been presented by *Germanovich et al.* [2009].

The turbine designs were proven suitable for use in both high-temperature focused flow and low-temperature diffuse flow areas. With TFM2 we obtained a minimum velocity of 2 cm/s at Grotto (measurements 6 and 9 in Table 3). To the best of our knowledge, this is the lowest flow rate ever measured at the JdF Ridge. We obtained a velocity of 198.6 cm/s with TFM1 at a black smoker on the Godzilla structure in the High Rise vent field (measurement 19 in Table 3). Therefore, the flow rate at JdF can be at least as low as 2 cm/s and at least as high as 199 cm/s.

Results obtained with our devices (Table 3) also represent the first direct heat output measurements at the High Rise hydrothermal field, Endeavour segment [*Germanovich et al.*, 2009; *Holden et al.*, 2009].

7. Discussion

It is useful to compare the flow measurements and heat outputs we obtained with estimates made using other means. At high-temperature vents, velocity measurements using the cup anemometer and turbine flowmeters ranged between 5.9 and 199 cm/s. These values are generally in line with other direct measurements. For example, for black smokers, particle tracking measurements at ASHES ranged between 20 and 90 cm/s [*Rona and Trivett*, 1992], between 10 and 30 cm/s at EPR 9°50′N [*Ramondenc et al.*, 2006], and between 1 and 5 m/s at EPR 21°N [*Macdonald et al.*, 1980]. Early turbine flowmeter measurements have ranged between 70 and 236 cm/s at EPR 21°N sites [*Converse et al.*, 1984] and between 68 and 337 cm/s on the Juan de Fuca Ridge [*Ginster et al.*, 1994]. Estimates of diffuse flow discharge have ranged from values as low as 1.1 and 4.9 mm/s at the substrate level at Lucky Strike [*Sarrazin et al.*, 2009], 5 mm/s at TAG [*Schultz et al.*, 1996], to 4 cm/s at EPR 9°50′N [*Ramondenc et al.*, 2006] and to 7–15 cm/s at the Peanut structure in the MEF [*Schultz et al.*, 1992]. These estimates of diffuse flow are generally similar to our measurements of low-temperature venting (focused or diffused), which ranged between 2 and 17.5 cm/s (Tables 1–4).

Comparison of heat output estimates is somewhat more difficult, however. For example, *Bemis et al.* [1993] found that the median heat flux per black smoker vent was 9 MW and 3 MW for the Endeavour (18 vents) and Southern (18 vents) segments, respectively, and the total heat flux from high-temperature venting at these JdF segments was estimated as 239 MW and 66 MW, respectively. *Ginster et al.* [1994] obtained heat outputs for individual black smoker vents ranging between 0.9 and 42 MW for the MEF with an average value of 6.2 MW/vent. In contrast, our measurements (Tables 2 and 3) obtained an average of 1.8 MW/vent at Hulk from 16 high-temperature ($T > 140$°C) focused vents and 1.3 MW/vent at Dante from 25 high-temperature focused vents. Four measurements on Dante with devices preceding our TFMs and cup anemometer (Table 1) resulted in the average heat output of 0.52 MW/vent. In general, it appears that our flow measurements show lower heat output than those obtained nearly two decades earlier by *Bemis et al.* [1993] and *Ginster et al.* [1994]. This may reflect the general decline in heat output in MEF. Measurements using Autonomous Benthic Explorer in 2000 yielded approximately 600 MW [*Veirs et al.*, 2006], whereas repeat measurements in 2004 yielded approximately 300 MW for MEF [*Thompson et al.*, 2005].

Our flowmeter measurements made at a high-temperature vent in the Dead Dog and Puppy Dog mounds in Middle Valley, JdF, resulted in advective heat outputs of 20 MW (measurement 27 in Table 3), 19 MW (measurement 28 in Table 3), and 0.41 MW (measurement 5 in Table 1), respectively. Using plume theory, *Stein and Fisher* [2001] measured the advective heat flux from 10 individual vents in Middle Valley (eight at Dead Dog and two at Bent Hill sites) to be in the range of 1.4–39.6 MW with the mean value of 9 MW. Our result is in agreement with *Stein and Fisher*'s [2001] range. Thermal anomalies registered by *Baker et al.* [1987] at the Dead Dog site were consistent with a 6.5 MW heat source, which may be representative of the advective heat flux in the Middle Valley approximately 25 years ago. The somewhat higher value measured by *Stein and Fisher* [2001] for the mean vent heat discharge may be indicative of the increased advective heat budget a decade later. In turn, the mean value of our measurements, 13 MW, may be an

indication that advective heat output at Middle Valley has continued to increase. It is difficult to determine definitely, however, based on our three measurements in two locations.

Ramondenc et al. [2006] presented the measurement results obtained in 2004, shortly before the 2005–2006 EPR eruption at 9°50′N [e.g., *Rubin et al.*, 2012]. Focused, high-temperature discharges were measured at structures Bio 9, M-vent, P-vent, and Tica both in 2004 [*Ramondenc et al.*, 2006] and 2014 (Table 4). In 2004, each of these structures had several orifices with a typical heat output of 1 MW per orifice. In 2014, M-vent and Tica did not have any high-temperature venting at all. P-vent had two white smokers and one grey with the mean heat output of 0.29 MW per orifice (Table 4). Venting at Bio 9 appears to have increased compared to the 2004 level, however, as the black smoker measurement obtained in 2014 also indicates a heat output of the order of 1 MW per high-temperature vent and, visually, the Bio 9 structure had several vigorous black smoker clusters. Overall, the high-temperature, advective heat output from Bio 9 is estimated to be tens of megawatts, which is several times greater than the 9 MW estimated in 2004 [*Ramondenc et al.*, 2006]. Furthermore, it appears that Bio 9 alone now vents at the same order of heat output as the entire 9°50′N hydrothermal field did in 2004 (42 MW). It is possible that the high-temperature, advective flow has become more channelized, predominately discharging through the Bio 9 structure.

Although our data are somewhat limited, they do provide some ground truth for flow estimates made using acoustic or optical methods described in section 2.2.2. For example, using acoustic scintillation methods, *Xu and Di Iorio* [2011] estimate the heat output at Dante to be approximately 62 MW. The data shown in Tables 2 and 3 represent only about half (and, possibly, less) of the vents on Dante. If the data are extrapolated to encompass all the high-temperature vents, the heat output obtained using the flowmeter data would be a minimum of 50 MW.

Finally, by making direct measurements of flow at both focused and diffuse flow vents, one can, in principle, obtain estimates of the partitioning between focused and diffuse flows [e.g., *Ramondenc et al.*, 2006] as well as estimates of geochemical transports in focused and diffuse flow settings [*Lowell et al.*, 2013]. For example, using an in situ mass spectrometer (ISMS), concentrations of CO_2(aq), CH_4, and H_2 were measured at a number of high-temperature and diffuse flow vents at MEF and Mothra [*Wankel et al.*, 2011] where we also made fluid flow and temperature measurements. The combination of the fluid flow and ISMS measurements showed that geochemical fluxes from diffuse flow sites could equal or exceed those from focused high-temperature sites and that the flux of H_2 from diffuse flow vents was much less than expected, suggesting utilization by biota [*Wankel et al.*, 2011].

8. Conclusions

We designed, built, and calibrated a cup anemometer and two turbine flowmeter devices for making direct measurements of both focused and diffuse fluid flows in seafloor hydrothermal systems. We have tested the devices with the manned submersible *Alvin* (30 dives) and ROV *Jason* (3 dives) and obtained 104 separate measurements conducted at depths up to 2511 m and at temperatures up to 363°C. In sea trials, the turbine flowmeters provided measurements of hydrothermal flow ranging between 2 and 198.6 cm/s. The cup anemometer device has operated successfully between 7.6 and 88.1 cm/s. The rate of 2 cm/s is the lowest ever measured at the JdF Ridge, and the results obtained with our devices (Table 3) represent the first direct heat output measurements at the High Rise hydrothermal field, Endeavour segment, and the Dead Dog vent area, Middle Valley, on the Juan de Fuca Ridge. The first direct measurements of the diffuse flow rates at most of the structures on the northern part of the Main Endeavour Field (Dante, Hulk, Grotto, and S&M) were also obtained with our devices.

The data reported by *Ramondenc et al.* [2006] for the EPR at 9°50′N is considerably expanded by the measurements reported in Table 4. This work also reports (Table 1) the first direct flow and heat measurements at the 9°39.5′N hydrothermal area on the East Pacific Rise, at the Tow Cam and ABE vent fields in the Lau Basin, and at the Puppy Dog mound in the Middle Valley. These measurements were obtained with devices that predated the flowmeters described in this work and were used in the process of their development.

The instruments we developed are simple, robust, small, lightweight, and self-contained devices that are able to measure quickly both high- and low-temperature fluid flows in a variety of hydrothermal settings. They are

easy to assemble, disassemble, and maintain. They require a significantly shorter amount of deployment time (usually a few minutes) for accurate measurements, than most of the previously developed instruments.

A particularly attractive feature of our flowmeters is their open bearing design (Figure 6). We did not notice any damage created by the accumulation of particles or chemical precipitates on the bearings even after many deployments as the open design allowed the fluids to flush through the system easily. This quality makes these devices, especially turbine flowmeters, promising for long-term deployment. Although the cup anemometer is simpler and easier to manufacture, our experience favors the turbine meters. For example, entrainment of the fresh sea water into the hydrothermal flow within the TFM devices is minimal compared to measurements with the cup anemometer. As a result of their robust modular design, the TFM devices could incorporate a variety of electronic sensors.

The new cup anemometer and TFM devices discussed in this paper provide reliable direct measurement results over a 2 orders of magnitude range of flow velocities and, hence, can be used to explore a broad range of heat and chemical fluxes at oceanic spreading centers. Such data are sorely lacking at present, and the availability of these devices for use on manned submersibles and ROVs fills an important niche in the arsenal of tools for understanding seafloor hydrothermal systems.

Acknowledgments

The authors appreciate the comments of Meg Tivey and an anonymous reviewer on an earlier version of this manuscript. The authors are indebted to Keir Becker, Monika Bright, Dave Butterfield, Chuck Fisher, Dan Fornari, Peter Girguis, Jim Holden, Daniela Di Iorio, George Luther, Ray Lee, Marv Lilley, Scott Nooner, Stefan Sievert, Martial Taillefert, and Karen Von Damm for accommodating our test program in their cruise schedules and for numerous onboard discussions of our devices that eventually led to the successful designs. They are particularly thankful to Daniela Di Iorio, Ray Lee, and Stefan Sievert for their continuous support and collaboration in measuring seafloor hydrothermal flow output. The authors are very grateful to *Alvin* pilots Pat Hickey, Bruce Strickrott, Sean Kelley, Mark Spear, Bob Waters, and Dave Walter and to *Jason* pilots Tito Collasius, Akel Kevis-Stirling, and Korey Verhein for many constructive suggestions and attention to detail that went far beyond their normal responsibilities. The authors greatly appreciate the help of Peter van Dyke and Pierre Ramondenc in designing the particle tracer device (Figure 1a), Larry Murdoch's help in designing the seepage meter (Figure 1b), and the help of Dennis Brown and Dennis Denney of GTRI Machine Services in manufacturing the TFM devices. L.N.G. is grateful to Joseph Ayoub, Dmitry Garagash, Larry Murdoch, Eric Olsen, Alexander Puzrin, Phil Roberts, Marvin Robinowitz, Peter Rona, Craig Taylor, Costa Vetriani, Guangyu Xu, and Wenyue Xu for their interest and many stimulating discussions. This research was supported by NSF grants OCE 0937057 (instrument development), OCE 0449578 (cruises AT15-34 and AT15-36), OCE 0732611 and 0731947 (cruise AT15-47), OCE 0623554 and 0623383 (cruise AT15-67) and OCE 1136727 (cruise AT26-10).

References

American Society for Testing and Materials (ASTM) (2010), *ASTM Standard A313/A313M–10e1, Standard Specification for Stainless Steel Spring Wire*, ASTM International, West Conshohocken, Pa., doi:10.1520/A0313_A0313M-10E01.

American Society for Testing and Materials (ASTM) (2011), *ASTM Standard B265–11, Standard Specification for Titanium and Titanium Alloy Strip, Sheet, and Plate*, ASTM International, West Conshohocken, Pa., doi:10.1520/B0265-11.

ASM (2005), *ASM Standard Handbook, Prop. and Sel.: Irons, Steels, and High Perform. Alloys*, vol. 1, ASM International, The Materials Information society, Materials Park, Ohio.

Baker, E. T. (1994), A 6-year time series of hydrothermal plumes over the Cleft segment of the Juan de Fuca Ridge, *J. Geophys. Res.*, *99*, 4889–4904, doi:10.1029/93JB01030.

Baker, E. T. (2007), Hydrothermal cooling of mid-ocean ridge axes: Do measured and modeled heat fluxes agree?, *Earth Planet. Sci. Lett.*, *263*, 140–150.

Baker, E. T., and G. J. Massoth (1987), Characteristics of hydrothermal plumes from two vent fields on the Juan de Fuca Ridge, northeast Pacific Ocean, *Earth Planet. Sci. Lett.*, *85*, 59–73.

Baker, E. T., G. A. Feely, and G. J. Massoth (1987), Hydrographic and chemical survey of hydrothermal plumes from the Middle Valley vent field, Juan de Puca Ridge, *Eos Trans. AGU*, *68*, 1325.

Baker, E. T., G. J. Massoth, S. L. Walker, and R. W. Embley (1993), A method for quantitatively estimating diffuse and discrete hydrothermal discharge, *Earth Planet. Sci. Lett.*, *118*, 235–249.

Baker, E. T., G. J. Massoth, R. A. Feely, G. A. Cannon, and R. E. Thomson (1998), The rise and fall of the CoAxial hydrothermal site, 1993–1996, *J. Geophys. Res.*, *103*, 9791–9806, doi:10.1029/97JB03112.

Baker, R. C. (1993), Turbine flowmeters: II. Theoretical and experimental published information, *Flow Meas. Instrum.*, *4*, 123–144.

Baker, R. C. (2000), *Flow Measurement Handbook: Industrial Designs, Operating Principles, Performance, and Applications*, Cambridge Univ. Press, Cambridge, U. K.

Bemis, K. G., R. P. Von Herzen, and M. J. Mottl (1993), Geothermal heat flux from hydrothermal plumes on the Juan de Fuca Ridge, *J. Geophys. Res.*, *98*, 6351–6365, doi:10.1029/92JB02273.

Bemis, K. G., P. A. Rona, D. Jackson, C. Jones, D. Silver, and K. Mitsuzawa (2002), A comparison of black smoker hydrothermal plume behavior at Monolith Vent and at Clam Acres vent field: Dependence on source configuration, *Mar. Geophys. Res.*, *23*, 81–96.

Butterfield, D. A., K. K. Roe, M. D. Lilley, J. A. Huber, J. A. Baross, R. W. Embley, and G. J. Massoth (2004), Mixing, reaction and microbial activity in the subseafloor revealed by temporal and spatial variation in diffuse flow vents at Axial Volcano, in *The Subseafloor Biosphere at Mid-Ocean Ridges*, *Geophys. Monogr.*, vol. 144, edited by W. S. D. Wilcock et al., pp. 269–289, AGU, Washington, D. C.

Camilli, R., D. Di Iorio, A. Bowen, C. M. Reddy, A. H. Techet, D. R. Yoerger, L. L. Whitcomb, J. S. Seewald, S. P. Sylva, and J. Fenwick (2011), Acoustic measurement of the Deepwater Horizon Macondo well flow rate, *Proc. Natl. Acad. Sci. U.S.A.*, *109*, 20,235–20,239.

Candelier, F., and O. Vauquelin (2012), Matched asymptotic solutions for turbulent plumes, *J. Fluid Mech.*, *699*, 489–499, doi:10.1017/jfm.2012.134.

Carazzo, G., E. Kaminski, and S. Tait (2008), On the rise of turbulent plumes: Quantitative effects of variable entrainment for submarine hydrothermal vents, terrestrial and extra terrestrial explosive volcanism, *J. Geophys. Res.*, *113*, B09201, doi:10.1029/2007JB005458.

Caulfield, C. P., and A. W. Woods (1995), Plumes with non-monotonic mixing behavior, *Geophys. Astrophys. Fluid Dyn.*, *79*, 173–199.

Converse, D. R. (1985), Flow rates in the East Pacific Rise (21°N) hot springs, and numerical investigations of two regimes of hydrothermal circulation, PhD thesis, 462 pp., Harvard Univ., Cambridge, Mass.

Converse, D. R., H. D. Holland, and J. M. Edmond (1984), Flow rates in the axial hot springs of the East Pacific Rise (21°N): Implications for the heat budget and the formation of massive sulfide deposits, *Earth Planet. Sci. Lett.*, *69*, 159–175.

Cooper, M. J., H. Elderfield, and A. Schultz (2000), Diffuse hydrothermal fluids from Lucky Strike hydrothermal vent field: Evidence for a shallow conductively heated system, *J. Geophys. Res.*, *105*, 19,369–19,375, doi:10.1029/2000JB900138.

Corliss, J. B., et al. (1979), Submarine thermal springs on the Galapagos Rift, *Science*, *203*, 1073–1083.

Crone, T. J., and M. Tolstoy (2010), Magnitude of the 2010 Gulf of Mexico oil leak, *Science*, *330*, 634.

Crone, T. J., R. E. McDuff, and W. S. D. Wilcock (2008), Optical plume velocimetry: A new flow measurement technique for use in seafloor hydrothermal systems, *Exp. Fluids*, *45*, 899–915, doi:10.1007/s00348-008-0508-2.

Cuthbert, M., and S. Beck (1999), A non-dimensional method to increase the accuracy of turbine flowmeters, *Proc. Inst. Mech. Eng., Part E*, *213*, 121–126.

Di Iorio, D., D. Lemon, and R. Chave (2005), A self-contained acoustic scintillation instrument for path-averaged measurements of flow and turbulence with application to hydrothermal vent and bottom boundary layer dynamics, *J. Atmos. Oceanic Technol.*, *22*, 1602–1617.

Di Iorio, D., J. W. Lavelle, P. A. Rona, K. Bemis, G. Xu, L. N. Germanovich, R. P. Lowell, and G. Genc (2012), Measurements and models of heat flux and plumes from hydrothermal discharges near the deep sea floor, *Oceanography*, *25*, 169–179.

Dymond, J., E. Baker, and J. Lupton (1988), Plumes: Ocean limb of seafloor hydrothermal systems, in *The Mid-Ocean Ridge—A Global Dynamic System, Proceedings of the Salishan Workshop*, pp. 209–231, National Academy Press, Washington, D. C.

Edmond, J. M., J. B. Corliss, and L. I. Gordon (1979), Ridge crest-hydrothermal metamorphism at the Galapagos spreading center and reverse weathering, in *Deep Drilling Results in the Atlantic Ocean: Ocean Crust*, *Ewing Ser.*, vol. 2, edited by M. Talwani, C. G. Harrison, and D. E. Hayes, pp. 383–390, AGU, Washington, D. C.

Fannelop, T. K., and D. M. Webber (2003), On buoyant plumes rising from area sources in calm environments, *J. Fluid Mech.*, *497*, 319–334.

Fischer, H. B., E. J. List, R. C. Y. Koh, J. Imberger, and N. H. Brooks (1979), *Mixing in Inland and Coastal Waters*, pp. 315–389, Academic Press, San Diego, Calif.

Futrell, J. C. (1989), Bucket wheel assembly for a flow measuring device, US Patent 4,866,985.

Gendron, J. F., J. F. Todd, R. A. Feely, E. T. Baker, and D. C. Kadko (1994), Excess ^{222}Rn above the Cleft segment of the Juan de Fuca Ridge, *J. Geophys. Res.*, *99*, 5007–5015, doi:10.1029/93JB03209.

Germanovich, L. N., D. Di Iorio, G. Genc, R. S. Hurt, R. P. Lowell, J. F. Holden, D. A. Butterfield, and E. J. Olson (2009), Direct measurements of hydrothermal heat output at Juan de Fuca Ridge, *Eos Trans. AGU*, *90*, Fall Meet. Suppl., Abstract OS13A-1179.

Germanovich, L. N., R. P. Lowell, and P. Ramondenc (2011), Magmatic origin of hydrothermal response to earthquake swarms: Constraints from heat flow and geochemical data, *J. Geophys. Res.*, *116*, B05103, doi:10.1029/2009JB006588.

Ginster, U., M. J. Mottl, and R. P. Von Herzen (1994), Heat flux from black smokers on the Endeavour and Cleft segments, Juan de Fuca Ridge, *J. Geophys. Res.*, *99*, 4937–4950, doi:10.1029/93JB02800.

Grafarend, E. W., and F. W. Krumm (2006), *Map Projections, Cartographic Information Systems*, 732 pp., Springer, Berlin.

Grey, J. (1960), Calibration of turbine meters for cryogenic operation, *Am. Rocket Soc. J.*, *30*, 192–193.

Hochreiter, H. M. (1958), Dimensionless correlation of coefficients of turbine type flow meters, *Trans. ASME*, *80*, 1363–1368.

Holden, J. F., D. A. Butterfield, and M. D. Lilley (2009), Endeavour-Axial Geochemistry and Ecology Research (EAGER), 2009 Cruise, R/V Atlantis–DSV *Alvin* AT15-47, Endeavour Segment and Axial Volcano, Juan de Fuca Ridge, Northeast Pacific Ocean, AT15-47 NeMO 2009 Cruise Report, 56 pp. [Available at http://www.marine-geo.org/link/data/field/Atlantis/AT15-47/docs/AT15-47_NeMO_2009_Cruise_Report_final.pdf.]

Hunt, G. R., and N. B. Kaye (2001), Virtual origin correction for lazy turbulent plumes, *J. Fluid Mech.*, *435*, 377–396.

Hunt, G. R., and N. B. Kaye (2005), Lazy plumes, *J. Fluid Mech.*, *533*, 329–338, doi:10.1017/S002211200500457X.

Hunt, G. R., and T. S. van den Bremer (2011), Classical plume theory: 1937–2010 and beyond, *IMA J. Appl. Math.*, *76*, 424–448, doi:10.1093/imamat/hxq056.

Insley, H., H. F. Mcmurdie, W. H. Parsons, and B. L. Steierman (1947), Some properties of materials used for jewel instrument bearings, *Am. Mineral.*, *32*(1–2), 1–15.

Jackson, D. R., C. D. Jones, P. A. Rona, and K. G. Bemis (2003), A method for Doppler acoustic measurement of black smoker flow fields, *Geochem. Geophys. Geosyst.*, *4*(11), 1095, doi:10.1029/2003GC000509.

Kaminski, E., S. Tait, and G. Carazzo (2005), Turbulent entrainment in jets with arbitrary buoyancy, *J. Fluid Mech.*, *526*, 361–376, doi:10.1017/S0022112004003209.

Kelley, D. S., et al. (2012), Endeavour segment of the Juan de Fuca Ridge: One of the most remarkable places on Earth, *Oceanography*, *25*(1), 44–61, doi:10.5670/oceanog.2012.03.

King, L. V. (1914), On the convection of heat from small cylinders in a stream of fluid: Determination of the convection constants of small platinum wires with applications to hot-wire anemometry, *Proc. R. Soc. London, Ser. A*, *214*, 373–432.

Lang, S. Q., D. A. Butterfield, M. D. Lilley, H. P. Johnson, and J. I. Hedges (2006), Dissolved organic carbon in ridge-axis and ridge-flank hydrothermal systems, *Geochim. Cosmochim. Acta*, *70*, 3830–3842.

Lee, W. F. Z., and H. Karlby (1960), A study of viscosity effects and its compensation on turbine-type flowmeters, *Trans. ASME J. Basic Eng.*, *82*, 717–728.

Liedtke, J., and M. Schatzmann (1997), Dispersion from strongly buoyant sources, Final Report, EUProject EV5V-CT-93-0262, Meteorological Institute, Univ. of Hamburg.

Little, S. A., K. D. Stolzenbach, and R. P. Von Herzen (1987), Measurements of plume flow from a hydrothermal vent field, *J. Geophys. Res.*, *92*, 2587–2596, doi:10.1029/JB092iB03p02587.

Liu, L., and R. P. Lowell (2009), Models of hydrothermal heat output from a convecting, crystallizing, replenished magma chamber beneath an oceanic spreading center, *J. Geophys. Res.*, *114*, B02102, doi:10.1029/2008JB005846.

Lowell, R. P., and L. N. Germanovich (1994), On the temporal evolution of high-temperature hydrothermal systems at ocean ridge crests, *J. Geophys. Res.*, *99*, 565–575, doi:10.1029/93JB02568.

Lowell, R. P., and L. N. Germanovich (2004), Seafloor hydrothermal processes: Results from scale analysis and single-pass models, in *Mid-Ocean Ridges: Hydrothermal Interactions Between the Lithosphere and Oceans*, *Geophys. Monogr. Ser.*, vol. 148, edited by C. R. German, J. Lin, and L. M. Parson, pp. 219–244, AGU, Washington, D. C.

Lowell, R. P., A. Farough, J. Hoover, and K. C. Cummings (2013), Characteristics of magma-driven hydrothermal systems at oceanic spreading centers, *Geochem. Geophys. Geosyst.*, *14*, 1756–1770, doi:10.1002/ggge.20109.

Macdonald, K. C. (1983), A geophysical comparison between fast and slow spreading centers: Constraints on magma chamber formation and hydrothermal activity, in *Hydrothermal Processes at Seafloor Spreading Centers*, edited by P. A. Rona et al., pp. 369–390, Plenum, N. Y.

Macdonald, K. C., K. Becker, F. N. Spiess, and R. D. Ballard (1980), Hydrothermal heat flux of the "black smoker" vents on the East Pacific Rise, *Earth Planet. Sci. Lett.*, *48*, 1–7.

Merzkirch, W. (2005), *Fluid Mechanics of Flow Metering*, Springer, New York.

Michauxa, G., and O. Vauquelin (2008), Solutions for turbulent buoyant plumes rising from circular sources, *Phys. Fluids*, *20*, 066601, doi:10.1063/1.2926758.

Middleton, J. H., and R. E. Thomson (1986), Modeling the rise of hydrothermal plumes, *Can. Tech. Rep. Hydrogr. Ocean Sci.*, *69*, 1–18.

Morton, B. R. (1959), Forced plume, *J. Fluid Mech.*, *5*, 151–163.

Morton, B. R., and J. Middleton (1973), Scale diagrams for forced plumes, *J. Fluid Mech.*, *58*, 165–176.

Morton, B. R., G. Taylor, and J. S. Turner (1956), Turbulent gravitational convection from maintained and instantaneous sources, *Proc. R. Soc. London, Ser. A*, *234*(1196), 1–23.

Munson, B. R., D. F. Young, and T. H. Okiishi (2005), *Fundamentals of Fluid Mechanics*, 5th ed., 816 pp., Wiley, New York.

Murton, B. J., L. J. Redbourn, C. R. German, and E. T. Baker (1999), Sources and fluxes of hydrothermal heat, chemicals and biology within a segment of the Mid-Atlantic Ridge, *Earth Planet. Sci. Lett.*, *171*, 301–317.

Ostashev, V. E., and D. K. Wilson (2015), *Acoustics in Moving Inhomogeneous Media*, 541 pp., CRC Press, Boca Raton, Fla.

Palmer, D. R. (2005), Acoustical scattering from constituents of an ocean plume located near a boundary surface, *Geosci. Remote Sens.*, *43*, 770–777.
Palmer, D. R., and P. A. Rona (2005), Acoustical imaging of deep ocean hydrothermal flows, in *Sounds of the Sea, From Ocean Acoustics to Acoustical Oceanography*, edited by H. Medwin, pp. 551–553, Cambridge Univ. Press, Cambridge, U. K.
Papanicolaou, P. N., and E. J. List (1987), Statistical and spectral properties of tracer concentrations in round buoyant jets, *Int. J. Heat Mass Transfer*, *30*, 2059–2071.
Ramondenc, P., L. N. Germanovich, K. L. Von Damm, and R. P. Lowell (2006), The first measurements of hydrothermal heat output at 9°50′N, East Pacific Rise, *Earth Planet. Sci. Lett.*, *263*, 140–150.
Rona, P. A. (1999), Deep-diving manned research submersibles, *Mar. Technol. Soc. J.*, *33*(4), 13–25.
Rona, P. A., and D. A. Trivett (1992), Discrete and diffuse heat transfer at ASHES vent field, Axial Volcano, Juan de Fuca Ridge, *Earth Planet. Sci. Lett.*, *109*, 57–71.
Rona, P. A., K. G. Bemis, D. Silver, and C. D. Jones (2002), Acoustic imaging, visualization, and quantification of buoyant hydrothermal plumes in the ocean, *Mar. Geophys. Res.*, *23*, 147–168.
Rooney, G. G., and P. F. Linden (1996), Similarity considerations for non-Boussinesq plumes in an unstratified environment, *J. Fluid Mech.*, *318*, 237–250.
Rosenberry, D. O. (2008), A seepage meter designed for use in flowing water, *J. Hydrol.*, *359*, 118–130.
Ross, T., and R. Lueck (2003), Sound scattering from oceanic turbulence, *Geophys. Res. Lett.*, *30*(6), 1343, doi:10.1029/2002GL016733.
Rubin, K. H., S. A. Soule, W. W. Chadwick Jr., D. J. Fornari, D. A. Clague, R. W. Embley, E. T. Baker, M. R. Perfit, D. W. Caress, and R. P. Dziak (2012), Volcanic eruptions in the deep sea, *Oceanography*, *25*(1), 142–157, doi:10.5670/oceanog.2012.12.
Rudnicki, M., and H. Elderfield (1992), Theory applied to the Mid-Atlantic Ridge hydrothermal plumes: The finite-difference approach, *J. Volcanol. Geotherm. Res.*, *50*, 161–172.
Sarrazin, J., P. Rodier, M. K. Tivey, H. Singh, A. Schultz, and P. M. Sarradin (2009), A dual sensor device to estimate fluid flow velocity at diffuse hydrothermal vents, *Deep Sea Res., Part I*, *56*, 2065–2074.
Schultz, A., J. R. Delaney, and R. E. McDuff (1992), On the partitioning of heat flux between diffuse and point source seafloor venting, *J. Geophys. Res.*, *97*, 12,299–12,314, doi:10.1029/92JB00889.
Schultz, A., P. Dickson, and H. Elderfield (1996), Temporal variations in diffuse hydrothermal flow at TAG, *Geophys. Res. Lett.*, *23*, 3471–3474, doi:10.1029/96GL02081.
Sharqawy, M. H., J. H. Lienhard V, and S. M. Zubair (2010), Thermophysical properties of seawater: A review of existing correlations and data, *Desalin. Water Treat.*, *16*(1–3), 354–380, doi:10.5004/dwt.2010.1079.
Snyder, J. P. (1997), *Map Projections—A Working Manual*, *Prof. Pap. 1395*, USGS, Washington, D. C., 1st ed. 1987, reprint 1989 and 1994 with corrections, reprint 1997, 383 pp.
Speer, K. G., and K. R. Helfrich (1995), Hydrothermal plumes: A review of flow and fluxes, in *Hydrothermal Vents and Processes*, edited by L. M. Parson, C. L. Walker and D. R. Dixon, *Geol. Soc. London Spec. Publ.*, *87*, 373–385.
Speer, K. G., and P. A. Rona (1989), A model of an Atlantic and Pacific hydrothermal plume, *J. Geophys. Res.*, *94*, 6213–6220, doi:10.1029/JC094iC05p06213.
Spiess, F. N., et al. (1980), East Pacific Rise: Hot springs and geophysical experiments, *Science*, *207*, 1421–1433.
Stein, J. S., and A. T. Fisher (2001), Multiple scales of hydrothermal circulation in Middle Valley, northern Juan de Fuca Ridge: Physical constraints and geologic models, *J. Geophys. Res.*, *106*, 563–580.
Sun, H., R. Feistel, M. Koch, and A. Markoe (2008), New equations for density, entropy, heat capacity, and potential temperature of a saline thermal fluid, *Deep-Sea Res. I*, *55*, 1304–1310, doi:10.1016/j.dsr.2008.05.011.
Tennekes, H., and J. L. Lumley (1972), *A First Course in Turbulence*, MIT Press, Cambridge, Mass.
Thompson, W. J., R. E. McDuff, F. R. Stahr, D. R. Yoerger, and M. Jakuba (2005), Heat flux from the Endeavour segment of the Juan de Fuca Ridge, *Eos Trans. AGU*, *86*(52), Fall Meet. Suppl., Abstract T31A–0489.
Thomson, R. E., J. R. Delaney, R. E. McDuff, D. R. Janecky, and J. S. McClain (1992), Physical characteristics of the Endeavour ridge hydrothermal plume during July 1998, *Earth Planet. Sci. Lett.*, *111*, 141–154.
Thomson, R. E., E. E. Davis, and B. J. Burd (1995), Hydrothermal venting and geothermal heating in Cascadia Basin, *J. Geophys. Res.*, *100*, 6121–6141, doi:10.1029/95JB00030.
Tivey, M. K., and S. Singh (1997), Non-destructive imaging of fragile sea-floor vent deposit samples, *Geology*, *25*, 391–394.
Tivey, M. K., E. Becker, R. Beinart, C. R. Fisher, P. R. Girguis, C. H. Langmuir, P. J. Michael, and A. L. Reysenbach (2012), Links from mantle to microbe at the Lau Integrated Study Site: Insights from a back-arc spreading center, *Oceanography*, *25*(1), 62–77, doi:10.5670/oceanog.2012.04.
Turner, J. (1986), Turbulent entrainment: The development of the entrainment assumption, and its application to geophysical flows, *J. Fluid Mech.*, *173*, 431–472.
Turner, J. S., and I. H. Campbell (1987), Temperature, density and buoyancy fluxes in "black smoker" plumes, and the criterion for buoyancy reversal, *Earth Planet. Sci. Lett.*, *86*, 85–92.
van den Bremer, T. S., and G. R. Hunt (2010), Universal solutions for Boussinesq and non-Boussinesq plumes, *J. Fluid Mech.*, *644*, 165–192.
van Veen, F. (1977), *Handbook of Stroboscopy*, 46 pp., Gen Rad Inc., Concord, Mass.
Vaughn, E. C., J. M. Fulford, and H. R. Myers (2006), Bucket wheel assembly for fluid flow meters, US Patent 7,017,425 B1.
Veirs, S. R., R. E. McDuff, and F. R. Stahr (2006), Magnitude and variance of near-bottom horizontal heat flux at the Main Endeavour hydrothermal vent field, *Geochem. Geophys. Geosyst.*, *7*, Q02004, doi:10.1029/2005GC000952.
Von Damm, K. L., and M. D. Lilley (2004), Diffuse flow hydrothermal fluids from 9°50′N East Pacific Rise: Origin, evolution and biogeochemical controls, in *The Subseafloor Biosphere at Mid-Ocean Ridges*, *Geophys. Monogr.*, vol. 144, pp. 245–268, AGU, Washington, D. C.
Wankel, S. D., L. N. Germanovich, D. L. Marvin, G. Genc, C. J. DiPerna, A. S. Bradley, E. J. Olson, and P. R. Girguis (2011), Influence of subsurface biosphere on geochemical fluxes from diffuse hydrothermal fluids, *Nat. Geosci.*, *4*, 461–468.
Webster, J. G. (1999), *The Measurement, Instrumentation, and Sensors Handbook*, Springer, New York.
Woods, A. W. (1997), A note on non-Boussinesq plumes in an incompressible stratified environment, *J. Fluid Mech.*, *345*, 347–356.
Woods, A. W. (2010), Turbulent plumes in nature, *Annu. Rev. Fluid Mech.*, *42*, 391–412.
Xu, G., and D. Di Iorio (2011), The relative effects of particles and turbulence on acoustic scattering from deep-sea hydrothermal vent plumes, *J. Acoust. Soc. Am.*, *130*, 1856.
Yoerger, D., J. Newman, and J. J. Slotine (1986), Supervisory control system for the *Jason* ROV, *IEEE J. Oceanic Eng.*, *11*(3), 392–400.